Spectrometry of charged particles from inertial-confinement-fusion plasmas

F. H. Séguin,[a] J. A. Frenje, C. K. Li, D. G. Hicks,[b] S. Kurebayashi, J. R. Rygg, B.-E. Schwartz, and R. D. Petrasso[c]
Plasma Science and Fusion Center, Massachusetts Institute of Technology, Cambridge, Massachusetts 02139

S. Roberts, J. M. Soures, D. D. Meyerhofer,[d] T. C. Sangster, J. P. Knauer, C. Sorce, V. Yu. Glebov, and C. Stoeckl
Laboratory for Laser Energetics, University of Rochester, Rochester, New York 14623

T. W. Phillips
Lawrence Livermore National Laboratory, Livermore, California 94550

R. J. Leeper
Sandia National Laboratories, Albuquerque, New Mexico 87185

K. Fletcher and S. Padalino
SUNY Geneseo Nuclear Structure Laboratory, State University of New York, Geneseo, New York 14454

(Received 24 April 2002; accepted 9 September 2002)

High-resolution spectrometry of charged particles from inertial-confinement-fusion (ICF) experiments has become an important method of studying plasma conditions in laser-compressed capsules. In experiments at the 60-beam OMEGA laser facility [T. R. Boehly *et al.*, Opt. Commun. **133**, 495 (1997)], utilizing capsules with D_2, D^3He, DT, or DTH fuel in a shell of plastic, glass, or D_2 ice, we now routinely make spectral measurements of primary fusion products (p, D, T, ^{3}He, α), secondary fusion products (p), ''knock-on'' particles (p, D, T) elastically scattered by primary neutrons, and ions from the shell. Use is made of several types of spectrometers that rely on detection and identification of particles with CR-39 nuclear track detectors in conjunction with magnets and/or special ranging filters. CR-39 is especially useful because of its insensitivity to electromagnetic noise and its ability to distinguish the types and energies of individual particles, as illustrated here by detailed calibrations of its response to 0.1–13.8 MeV protons from a Van de Graaff accelerator and to p, D, T, and α from ICF experiments at OMEGA. A description of the spectrometers is accompanied by illustrations of their operating principles using data from OMEGA. Sample results and discussions illustrate the relationship of secondary-proton and knock-on spectra to capsule fuel and shell areal densities and radial compression ratios; the relationship of different primary fusion products to each other and to ion temperatures; the relationship of deviations from spherical symmetry in particle yields and energies to capsule structure; the acceleration of fusion products and the spectra of ions from the shell due to external fields; and other important physical characteristics of the laser-compressed capsules.
[DOI: 10.1063/1.1518141]

I. INTRODUCTION

Charged-particle spectrometry is an important method for studying inertial-confinement-fusion (ICF) plasmas, because of the close relationship between plasma conditions and particle spectral characteristics.[1–37] In a ''direct-drive'' ICF experiment, such as those at the 60-beam OMEGA laser facility,[38] a small capsule containing an appropriate fuel is directly illuminated by many laser beams which deposit energy on the capsule shell during a short time interval. The laser energy ablates away the outer part of the capsule shell (or ''ablator''), driving the remainder of the shell inward. The result is compression or implosion of the fuel, which reaches temperatures and densities necessary for fusion reactions. In addition to neutrons, these reactions produce charged particles whose numbers and energy spectra are directly related to the properties of the compressed plasmas formed by the high-density, ionized fuel and the ionized shell. Their spectra provide direct information about primary yields, fuel and shell temperatures, fuel and shell areal densities, implosion symmetry, and external electric fields in specific experiments, as well as information of general interest on such topics as the slowing down of energetic ions in plasmas.

The spectra of charged particles contain discrete lines and continua of protons, deuterons, tritons, ^{3}He, and alphas,

[a]Electronic mail: seguin@psfc.mit.edu
[b]Presently at Lawrence Livermore National Laboratory, Livermore, CA 94550
[c]Also a Visiting Senior Scientist, Laboratory for Laser Energetics, University of Rochester, Rochester, NY 14623.
[d]Also with Departments of Mechanical Engineering and Physics, and Astronomy, University of Rochester, Rochester, NY 14623.

generated mostly by thermonuclear reactions and by elastic scattering by fusion neutrons (''knock-on'' processes), with energies ranging from a few keV to 31 MeV. Most of these particles are generated mostly during a short ''burn'' interval, which is ~150 ps long at OMEGA. In addition, ions with energies up to about 1.4 MeV are generated by laser–plasma interactions in the shell of direct-drive ICF target capsules.[32] A list of specific charged particles of interest in ICF experiments is presented in Sec. II.

Detectors for these charged particles in spectrometers must meet a number of requirements including high detection efficiency, large dynamic range, good energy resolution, insensitivity to background radiation (neutrons, x rays and γ rays), and insensitivity to electromagnetic noise. Some work has been done with scintillation counters (obtaining spectral information via time-of-flight);[1,3–6,11,13,17] with nuclear emulsions;[20] and with LR115 cellulose nitrate track detectors,[2] pin diodes,[14] or charge-coupled devices[27,39] in conjunction with a magnet. CR-39 nuclear track detectors[40–48] have been used in most recent ICF applications,[7–10,12,14–16,19,21–25,27,29–37] and the object of this article is to provide a technical description of the specific methods that have been developed for a wide range of applications at OMEGA.[14,19,27,29–37] To maximize the utility of CR-39 in these applications, a detailed study of its response to charged particles has been undertaken utilizing particles from an accelerator and particles from OMEGA experiments as described in Sec. III. The design of spectrometers based on CR-39 is outlined in Sec. IV, and the use and utility of these instruments is described with representative data from a range of ICF experiments at OMEGA in Secs. V and VI.

TABLE I. Processes producing charged particles from imploded capsules. Asterisks indicate particles for which spectra have been measured with the techniques discussed in this article; some examples are shown in Sec. V.

Process type	Process and Result	
Primary	$D+D\rightarrow T^*[1.01\ MeV]+p^*[3.02\ MeV]$	(1)
	$D+D\rightarrow n[2.45\ MeV]+{}^3He^*[0.82\ MeV]$	(2)
	$D+T\rightarrow \alpha^*[3.5\ MeV]+n\ [14.1\ MeV]$	(3)
	$T+T\rightarrow \alpha^*[\leq 6.6\ MeV]+2n\ [\leq 10.6\ MeV]$	(4)
	$D+{}^3He\rightarrow \alpha^*[3.6\ MeV]+p^*[14.7\ MeV]$	(5)
	$T+{}^3He\rightarrow \alpha[4.8\ MeV]+D^*[9.5\ MeV]$ (~43%)	(6)
	$T+{}^3He\rightarrow \alpha+p+n+12.1\ MeV$ (~51%)	(7)
	$T+{}^3He\rightarrow {}^5He[2.4\ MeV]+p\ [11.9\ MeV]$ (~6%)	(8)
Secondary[a]	${}^3He[\leq 0.82\ MeV]+D\rightarrow \alpha[6.6–1.7\ MeV]+p^*[12.6–17.5\ MeV]$	(9)
	$T[\leq 1.01\ MeV]+D\rightarrow \alpha[6.7–1.4\ MeV]+n[11.9–17.2\ MeV]$	(10)
	$n[14.1\ MeV]+p\rightarrow n'+p^*[\leq 14.1\ MeV]$	(11)
	$n[14.1\ MeV]+D\rightarrow n'+D^*[\leq 12.5\ MeV]$	(12)
	$n[14.1\ MeV]+T\rightarrow n'+T^*[\leq 10.6\ MeV]$	(13)
	$n[14.1\ MeV]+{}^3He\rightarrow n'+{}^3He^*[\leq 10.6\ MeV]$	(14)
	$n[2.45\ MeV]+p\rightarrow n'+p^*[\leq 2.45\ MeV]$	(15)
	$n[2.45\ MeV]+D\rightarrow n'+D[\leq 2.18\ MeV]$	(16)
	$n[2.45\ MeV]+T\rightarrow n'+T[\leq 1.84\ MeV]$	(17)
	$n[2.45\ MeV]+{}^3He\rightarrow n'+{}^3He[\leq 1.84\ MeV]$	(18)
Tertiary[b]	$D[\leq 12.5\ MeV]+{}^3He\rightarrow \alpha+p[\leq 30.8\ MeV]$	(19)
Laser–plasma interaction	Ablator protons* [≤~1.4 MeV] Nonhydrogenic ablator ions* [depending on shell material]	

[a]Reaction (9) is preceded by reaction (2), reaction (10) is preceded by reaction (1), reactions (11)–(14) are preceded by reaction (3), and reactions (15)–(18) are preceded by reaction (2).
[b]Reaction (19) is preceded by reactions (3) and (12).

II. CHARGED PARTICLES FROM ICF IMPLOSIONS

The fuel capsules in most current OMEGA experiments contain some combination of deuterium, tritium, ^{3}He, and occasionally hydrogen, in gas form (at pressures up to about 20 atm), within a thin, spherical shell at room temperature. The shell is usually made of either plastic (CH) or glass, though occasionally part or all of it is made of deuterated plastic (CD). The capsules are typically about 1 mm in diameter, and the shell thickness varies from a few μm to 33 μm. Cryogenic D_2-filled capsules with D_2-ice shells and a thin CH outer layer are also beginning to be used.[49] After exposure to a laser pulse of order 1 ns long, depositing of order 23 kJ of energy, the capsules are compressed to 1/10 or less of their original diameters. The fuel reaches a temperature of several keV and a density of order 10^{24} ions/cm^3.[50] Charged particles from these capsules include products of primary, secondary, and tertiary fusion reactions; ''knock-on'' ions from the fuel or shell that have been elastically scattered by primary neutrons, and ions from the ablator plasma. Table I lists many of the processes and particles of interest, while examples of measured spectra and demonstration of diagnostic use will be presented in Secs. V and VI.

Primary fusion reactions can produce charged particles through reactions (1)–(8) in Table I, depending on the fuel constituents. The yields of the different products are determined by the fusion rate coefficients shown in Fig. 1, which vary with ion temperature. The spectra of the charged primary fusion products have discrete lines at well-defined birth energies. The measured yields of these particles provide fundamental information about implosion performance (the temperatures and densities reached). The measured energies indicate how much energy was lost by the particles while passing out of the target capsule, and therefore give information about the burn-averaged fuel and shell areal density, or $\langle \rho R \rangle$, as will be discussed in Sec. VI.

Secondary fusion products result from sequential reactions in which energetic primary products of reactions (1) or (2) undergo fusion reactions with thermal deuterons in the fuel. Reactions (9) and (10) produce secondary particles with spectra which are spread over significant energy intervals because of the kinetic energy of the primary reactants (Fig. 2 illustrates a secondary-proton birth spectrum). The yields (typically of order 10^{-3} per primary reaction) and the mean energies can be used to study the burn-averaged fuel and shell $\langle \rho R \rangle$.[16,18,22,34]

When the fuel contains D and T, charged knock-on particles are generated by elastic scattering of 14.1 MeV DT neutrons with the surrounding fuel and shell material through the secondary processes (11)–(14). The energy spectra of the scattered particles are continua, with upper endpoints determined by kinematics; the shapes of the birth spectra are shown in Fig. 3. Scattered deuterons and tritons from the fuel

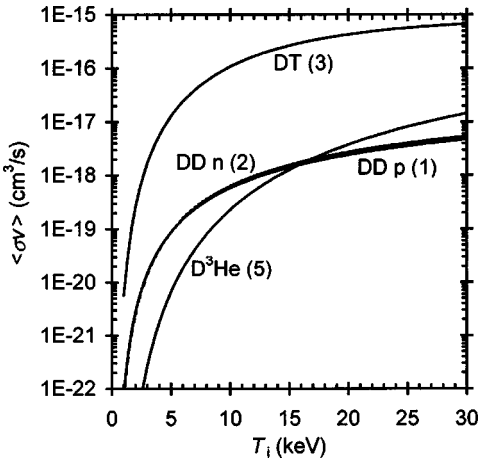

FIG. 1. Rate coefficients for the most important primary fusion reactions listed in Table I, referred to here by reaction number. The coefficients were calculated according to Ref. 51.

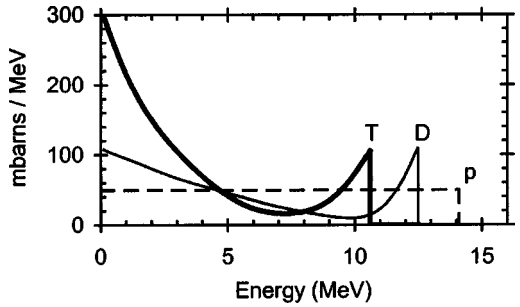

FIG. 3. Differential cross sections for elastic scattering of 14.1 MeV neutrons on protons, deuterons, and tritons (adapted from Ref. 52), where the energy is the scattered ion energy. The spectra of scattered particles emerging from an ICF capsule should have similar shapes, but will be distorted by energy loss in the plasma. For deuterons and tritons, the yield will be characterized here by the integral under the high-energy peak, from the energy where the yield is a minimum to the high-energy endpoint. For protons, the yield will be characterized by the number of particles per MeV.

have energies reaching 12.5 and 10.6 MeV, respectively, while scattered protons from the shell (if the shell contains hydrogen) reach 14.1 MeV. The yields of the knock-on deuterons and tritons are proportional to the burn-averaged fuel $\langle \rho R \rangle$,[7,10,15,33] while the knock-on protons give information about the burn-averaged shell $\langle \rho R \rangle$.[33] The knock-ons have yields 3–4 orders of magnitude below the yields of the primary products for OMEGA conditions.

Tertiary fusion products can also result from the three sequential reactions (3), (12), and (19), producing protons with energies reaching 31 MeV.[26,28] These reactions are not relevant for current OMEGA experiments because of low yields, but they could be useful with the higher yields expected in the future because they can pass out of a capsule with very high areal density and provide diagnostic information in situations where lower-energy protons cannot.

The spectrum below 1 MeV is usually dominated by charged particles from the shell plasma that have been accelerated to energies as high as 1.4 MeV.[32] These accelerations are due to hot-electron-producing laser-plasma interactions in the target corona which generate transient electric fields via charge separation. Charged fusion products passing through the corona when such fields are present have been observed to be accelerated by up to several hundred keV (as discussed in Sec. VI A, this is not an issue for "ICF-relevant" capsules).

In summary, we see that study of the charged particles tabulated in Table I requires sensitivity to protons up to about 18 MeV (or 31 MeV, for tertiary protons); deuterons up to 13 MeV, tritons and ^{3}He to 11 MeV, and alphas to at least 7 MeV. In Secs. III and IV we describe how this is done.

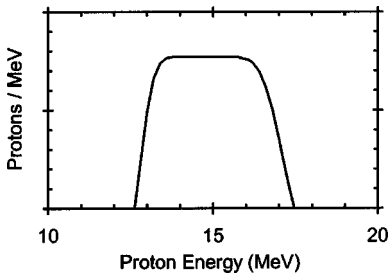

FIG. 2. A simulated birth spectrum of secondary protons from a D plasma. This curve was generated by assuming that primary 0.83 MeV ^{3}He from reaction (2) do not escape the fuel, but either slow down to thermal energies through interactions with the plasma or generate secondary protons through reaction (9) (see Ref. 34 for other scenarios, in which the shape of the spectrum does not deviate much from that shown here).

III. CHARGED-PARTICLE DETECTION WITH CR-39

A. Interaction of charged particles with CR-39

CR-39[40–48] is a clear plastic whose chemical composition is $C_{12}H_{18}O_7$. When a charged particle passes through, it leaves a trail of damage along its track in the form of broken molecular chains and free radicals. The amount of local damage along the track is related to the local rate at which energy is lost by the particle (dE/dx, where x is distance along the track). The length of the track is the range of the particle in the plastic. Particle tracks can be made visible by etching the CR-39 in NaOH. The surface of the plastic is etched away at a "bulk etch rate" V_B, while damaged material along particle tracks etches at a faster "track etch rate" V_T. If the particle entered normal to the plastic surface, the result is a conical pit with a sharply defined, round entrance hole and a pointed bottom. With increased etching time, the diameter and depth of the pit increase as long as the depth remains smaller than the total length of the track. This pit then shows where the particle entered, and its diameter provides a measure of dE/dx for the particle.

Since dE/dx is different for particles of a given type but different energies, the diameter provides a measure of incident energy. dE/dx is also different for different particle types, so diameters can often be used to identify the particle type if the energy is known. In either case, it is necessary to have a well-defined method for measuring the dimensions of the pits (generally called tracks) and a well-defined relationship between measured dimensions and particle characteristics.

In the following subsections we discuss how these measurements were made and how their relationship to particle properties was determined through calibration experiments

in which CR-39 was exposed to particles of known properties, either from an accelerator or from an ICF experiment. The sources of noise in CR-39 data are discussed, together with methods of minimizing the effects of noise on data analysis. Finally, the detection efficiency for different charged particles under practical circumstances is discussed. The characteristics of CR-39 can vary slightly according to fabrication methods; the material used here was the product of Track Analysis Systems Limited.[53]

B. Processing CR-39

Track diameters after etching depend on the NaOH molarity, the NaOH temperature, and the etch time. It is desirable to choose these parameters for optimal detectability of tracks, using the fact that larger track diameters and depths generally result from larger values of the ratio V_T/V_B. In the work described here, a molarity of 6.0 is used because V_T/V_B peaks at concentrations of ~6.25 molar NaOH (at temperatures above 60 °C).[44] The etch-rate ratio rises monotonically with temperature, and we use a temperature of 80 °C maintained in glass tubes in a thermostatically controlled water bath. The etch time is 6 h unless otherwise noted; shorter etch times are occasionally used to restrict track diameters at high particle densities in order to reduce track overlap.

For repeatable results, the etch parameters must be tightly controlled. A check on consistency is incorporated by exposing a small, signal-free area on the backside of each piece of CR-39 to 5.5 MeV alphas (from a 0.1 μCu ^{241}Am source) prior to etching. The tracks of these alphas should always etch to the same diameter, and if they don't (due to variations in either etch conditions or CR-39 characteristics) corrections can be made to other measured diameters by appropriate scaling.

After being etched, rinsed, and dried, the CR-39 is inspected on an optical microscope with transmission lighting and infrared-blocking filters. The area that must be studied is usually large, so a computer-driven scan of many microscope frames is used. The microscope objective generally has a magnification of 20; higher magnification gives better spatial resolution but greatly increases the time required to study a useful area of CR-39. Digital images (such as that shown in Fig. 4) are captured by a charge coupled device (CCD) camera. The camera in use for this study has 640×480 pixels, each of which corresponds to an area of 0.64 μm×0.64 μm in the focal plane with a 20× objective (a planned upgrade to a higher-resolution camera will increase the information content of images). Consistent microscope focus is critical, and the optimum relationship between the focal plane and the CR-39 surface should be maintained within a few microns.

Image analysis is performed in software. Our requirements for track characterization are simplified by the fact that our applications involve particles entering the CR-39 on trajectories normal to the surface, so tracks are nominally circular (for a different approach geared to tracks of particles entering obliquely, see Ref. 46). Tracks appear as dark circles on a light background; the perimeter of each track is identified as the location at which the image intensity drops below

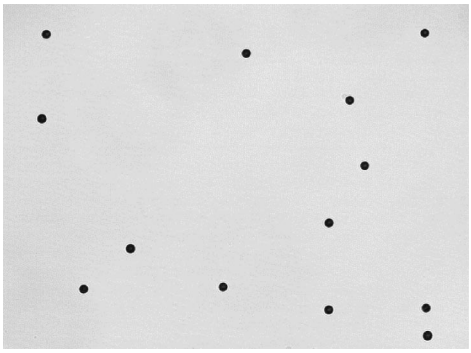

FIG. 4. A digitized microscope image of 2.01 MeV proton tracks in etched CR-39. The physical area represented by the image is 0.41 mm×0.31 mm, and the image itself has 640×480 pixels.

a specified "boundary threshold," for which we typically use 85% of the median background intensity. In addition to the location of each track, three other parameters are recorded: the diameter, the optical contrast, and the eccentricity. The diameter is calculated from the track area, and is of paramount importance because of its relationship to particle energy. The optical contrast is calculated as the deviation from background brightness as a percentage of background brightness. The contrast is important partly because it sometimes gives information about the energy of the particle (see below) and partly because it helps differentiate between real particle tracks (which tend to be dark) and false events (which are often lighter in appearance). Eccentricity can be calculated from the shape of the boundary in a number of ways, to quantify deviation from circularity. This information is useful for identifying multiple events (two or more tracks that touch each other) and for discriminating against debris and defects that have noncircular shapes.

C. Accelerator-based calibration of CR-39 response to protons

1. Track diameters

The response of CR-39 to protons with energies up to 13.8 MeV was studied at the 2 MeV Van de Graaff accelerator at the SUNY Geneseo Nuclear Structure Laboratory using the experimental setup shown in Fig. 5. Individual pieces of CR-39, each exposed to protons with one energy, were processed as described above (exposure to 5.5 MeV alphas, etching, and scanning with a microscope). To account for modest variations in etching conditions, the diameter of each track was multiplied by the ratio of the reference-alpha-track diameter for the sample piece to the reference-alpha-track diameter averaged over all pieces. Figure 6 shows the measured dependence of track diameter on incident proton energy. Tracks were seen and quantified for proton energies up to 9.3 MeV. The curve peaks at about 0.7 MeV, where proton tracks have diameters of about 20 μm (for the etch conditions described above). A model described in Refs. 43 and 29 was used to fit the experimental data, and the result is shown as the solid line in Fig. 6. The details of the model are not important here; it is used only to provide a smooth function that will represent the empirical relationship between proton energy and track diameter.

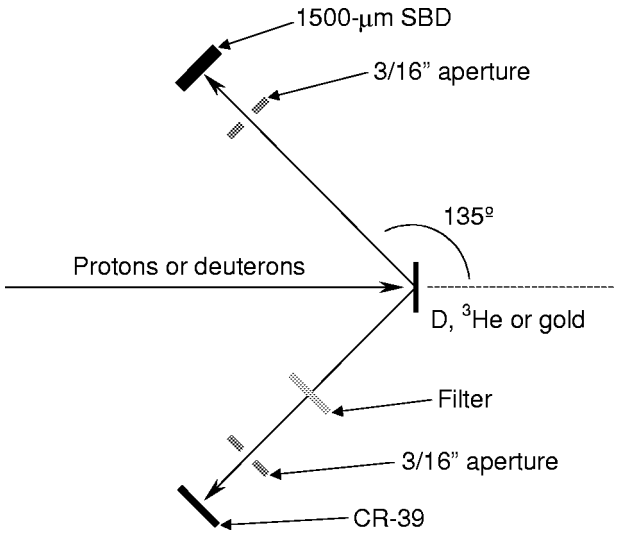

FIG. 5. The experimental setup used to expose samples of CR-39 to monoenergetic protons in the range 0.1–13.8 MeV. An accelerator beam of either protons or deuterons impinged on a target containing either gold, deuterium, or ^{3}He; protons emitted from the target at an angle of 135° from the initial beam direction were selected by two 3/16 in. diam apertures, each placed about 9 cm from the target. A surface barrier detector (SBD) was mounted behind one of the apertures, to monitor proton flux and energy, while a CR-39 detector was exposed behind the other aperture. Low-energy protons, from 0.1 to 1.3 MeV, were produced via Rutherford backscattering of accelerator protons on a gold target; the accelerator beam energy was varied to produce the desired energy of backscattered proton at the detectors. Protons with energies of 1.3–2.5 MeV were produced by making 2.5 MeV protons via the D(D,T)p reaction, initiated with 450 keV deuterons on a deuterium target, and then ranging down the energy as required with aluminum and Mylar filters. Protons with energies of 2.5–13.8 MeV were produced by making 13.8 MeV protons via the D(^{3}He,α)p reaction with a ^{3}He target, and ranging down the energy as required with filters. In most cases, the SBD was used to directly measure the proton energy as incident on the CR-39 by covering it with a duplicate of any filter placed in front of the CR-39. When this was not possible, energy loss due to filters was calculated with the program TRIM (Refs. 54 and 55).

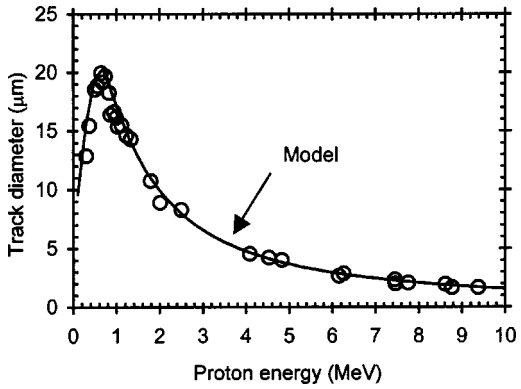

FIG. 6. Measured diameters of tracks in CR-39 for accelerator-generated protons with energies ranging from 0.3 to 9.3 MeV. The solid line is the best fit to the data using the model described in Refs. 43 and 29. From the fit, a bulk etch rate of 2.0 ± 0.1 μm/h was estimated for 6.0 molarity NaOH held at 80 °C. The dependence of dE/dx for protons in CR-39 has a form similar to the model fit, except that the peak value (at the Bragg peak) is at a lower energy (about 0.1 MeV).

2. Track contrast

The curve in Fig. 6 gives a diameter for each proton energy, but does not give a unique energy for each diameter. It turns out that it is often possible to discriminate between tracks of the same diameter but different energies on the basis of the optical contrast of the tracks; the track of the lower-energy particle is generally shallower and is less black in a microscope image. This is illustrated in Fig. 7, which is a contour plot of the number of detected tracks as a function of track diameter and track contrast for an experiment in which 13.8 MeV protons from the accelerator passed through an aluminum filter shaped like a wedge before hitting a piece of CR-39. The filter thickness varied from 400 to 1800 μm, with the result that the CR-39 was exposed to protons of all energies between 0 and 10.7 MeV. The figure shows a clear separation between two classes of tracks in the diameter interval 7–17 μm, corresponding to the two sides of the peak in the diameter-versus-energy curve in Fig. 6.

The contrast characteristics illustrated in Fig. 7 are not universal, because they correspond to a microscope with specific optical adjustments and a CCD camera with a specific linearity characteristic (and are also affected by etch conditions). Such plots need to be generated for each microscope system, and used to determine the contrast limits that can be used without missing tracks of a given diameter. As we will discuss below, this is important for many applications that result in a mixture of real data and noise. It is then desirable to use the tightest possible contrast limits to minimize noise, while taking care to avoid losing real data.

3. Track eccentricity

There are different ways to quantify the eccentricity of particle tracks in CR-39. For purposes of this discussion, we will define it as the ratio

$$\text{Eccentricity} \equiv \frac{\sqrt{\left[\int dr \int d\theta \nu(r,\theta) \sin 2\theta\right]^2 + \left[\int dr \int d\theta \nu(r,\theta) \cos 2\theta\right]^2}}{\int dr \int d\theta \nu(r,\theta)}, \tag{20}$$

where $\nu(r,\theta)$ is 1 everywhere inside the track and zero outside, and r and θ are polar coordinates defined with respect to the ''center of mass'' of the track. Large eccentricity can indicate that a track is due to a particle that did not impact the CR-39 normal to the surface; that tracks of two or more particles overlap; or that an apparent track is not due to a particle (but to debris or other surface imperfections). Since processed images of the CR-39 are digitized, small tracks that should be perfectly circular can appear to be eccentric due to the finite number of pixels defining them. Illustrated

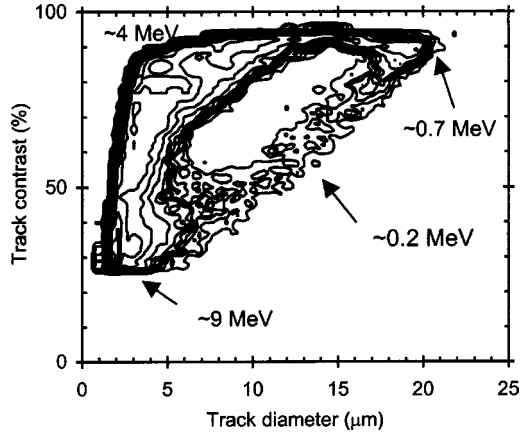

FIG. 7. Contour plot of the number of proton tracks vs. track diameter and optical contrast for protons spanning the energy range 0–10.7 MeV (tracks with contrast below 25% were not recorded, because in that range intrinsic noise dominates). Beginning at the large concentration of tracks at about 2 μm diameter and 30% contrast, corresponding to the highest energies shown in Fig. 6, the progression clockwise along the concentration of tracks corresponds to decreasing proton energy. There is a clear separation of tracks due to protons with energies above and below the diameter peak shown in Fig. 6.

in Fig. 8, this effect will become less important with a higher-resolution camera.

D. ICF-based calibration of CR-39 response to deuterons, tritons, and alphas

The response of CR-39 to deuterons, tritons, and alpha particles (as well as protons) has been tested by using particles generated in ICF experiments at OMEGA, through reactions (1), (5), (12), and (13). The energy of the particles was determined by their trajectories in the magnet-based spectrometers discussed in Sec. IV, although the particles also passed through a filter in front of the CR-39 and the program TRIM[54,55] was used to determine how much energy was lost before the particles hit the detector. Figure 9 shows the diameter as a function of incident energy for these particles. More details of these experiments, and the physics implications of the measurements, are discussed below in Sec. V.

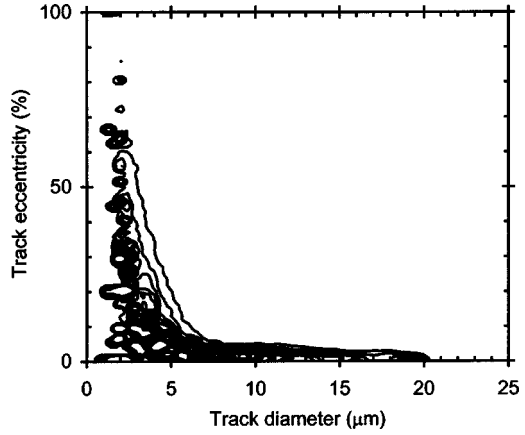

FIG. 8. Contour plot of the number of proton tracks vs. track diameter and track eccentricity for protons spanning the energy range 0–10.7 MeV, where eccentricity is defined in Eq. (20). For diameters larger that about 7 μm, the measured eccentricity reflects the true eccentricity of a track. At smaller diameters, the measured eccentricity is dominated by the effects of finite pixel size (in this case, about 0.64 μm/pixel; the measured eccentricity for small tracks is lower with smaller pixel sizes).

E. Sources of noise and background signal in CR-39 data

In applications of CR-39 on OMEGA, we find several types of tracks that do not represent the particles we are trying to study. These contribute noise to the measurements, and since all of the ''noise'' events are counted as positive events they add up to a background level that must be subtracted from the total number of tracks. The sources of noise discussed below are not intrinsically position dependent, so the background is usually assumed constant over the active area of a piece of CR-39 (subject to statistical fluctuations). It is frequently necessary to measure the background as a function of track diameter, because data analysis sometimes involves the use of different diameter ranges at different positions on the CR-39 (this will be seen in Figs. 21, 23, and 24).

1. "Intrinsic" noise and debris

One type of noise is due to defects in the CR-39 that look similar to real particle tracks after etching; we call this intrinsic noise. In addition, images of CR-39 sometimes include structure due to dust or debris on the surface (sometimes debris is generated when the CR-39 is cut to the desired size before use). It is sometimes hard to discriminate against intrinsic noise by eye, and since automatic computer processing of images is desirable the issue of automatic identification arises. Up to several hundred intrinsic noise tracks per cm^2 can sometimes be seen in the CR-39 material with typical contrast thresholds, and this becomes a problem when the number of particles to be studied is small. Some of the intrinsic noise tracks are shallow, resulting in a fairly low optical contrast. Figure 10 shows the intrinsic noise for four different unexposed CR-39 detectors, etched as described above, as a function of optical contrast threshold. It can be seen that the number of recorded events increases as the contrast threshold is reduced.

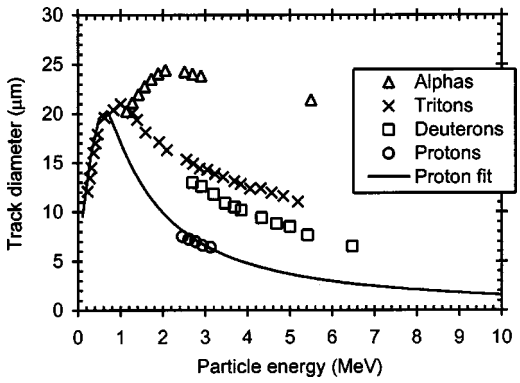

FIG. 9. Measured CR-39 track diameter as a function of incident energy for charged particles from OMEGA experiments, including D ^{3}He alphas, DD tritons, knock-on tritons, knock-on deuterons, and DD protons. The ''proton model fit'' curve comes from the fit to accelerator proton data in Fig. 6. (The 5.5 MeV alpha point was from a 0.1 μCu ^{241}Am source.)

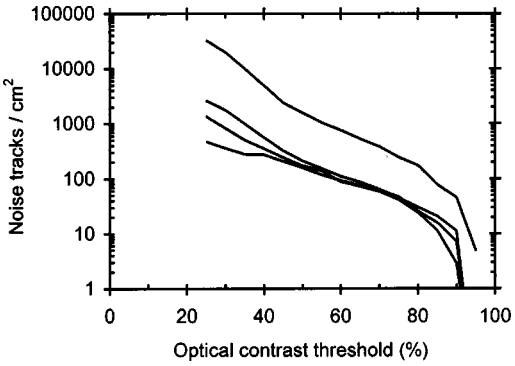

FIG. 10. The number of intrinsic noise tracks with optical contrast exceeding a given threshold, for several representative pieces of CR-39 (an eccentricity limit of 15% was used).

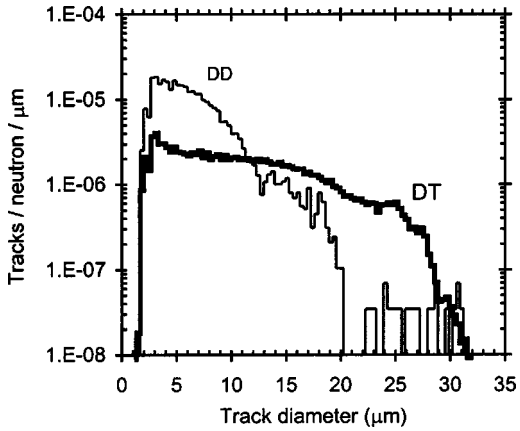

FIG. 11. Diameter histograms for tracks produced in CR-39 by DD and DT neutrons from OMEGA D_2 implosion 20250 and DT implosion 20 258. The track selection parameters used here were eccentricity $\leqslant$15% and contrast $\geqslant$65%.

2. Neutron-induced noise

Neutrons are produced in many of the reactions that produce the charged particles of interest here, and they interact with CR-39 via elastic scattering to produce recoil particles such as protons, carbon nuclei, and oxygen nuclei. From 14.1 MeV neutrons, charged particles can also be created in the CR-39 through nuclear reactions such as (n,p), (n,α), and $(n,2\alpha)\alpha$. These charged recoil particles and reaction products can produce tracks in etched CR-39 that are indistinguishable from those due to the charged ICF reaction products under study. To determine the precise nature of this neutron-induced noise in our implementation of CR-39, we recently completed a detailed study of its response to DD and DT neutrons from implosions at OMEGA.[56] Figure 11 shows diameter histograms for tracks in CR-39 due to neutron-induced events in two typical experiments. For DD implosions, the histogram is dominated by tracks due to recoil protons with energies up to 2.5 MeV, with track diameters up to 20 μm. For DT implosions, the diameter histogram includes recoil proton tracks with diameters up to about 20 μm; but there are other tracks with diameters exceeding the 20 μm maximum due to protons. This indicates that DT neutrons produced alpha particles and recoil carbon and oxygen ions, in addition to recoil protons, by interacting with the CR-39. The alpha particles produce tracks up to about 25–26 μm, while the carbon and oxygen nuclei produce tracks that are even larger.

With our standard etch conditions, it was found that the detection efficiencies for DD and DT neutrons are about 1.1×10^{-4} and 4.0×10^{-5}, respectively, on the CR-39 front side if counted tracks are limited to those with contrast $\geqslant$65% and eccentricity $\leqslant$15% (we note that the number of neutron-induced tracks seen on the front surface grows linearly with etch time; since recoil particles are scattered preferentially in the forward direction, the volume of CR-39 producing scattered particles seen at a given depth is proportional to that depth.). These results are in approximate agreement with other studies.[57] Since the yields of primary charged particles in the ICF experiments are generally comparable with the primary neutron yields, the neutron-generated ''noise'' or background is only 10^{-4} of the signal from the primary particles and not very important. But secondary fusion products [Eqs. (9) and (10)] and knock-on particles [Eqs. (11)–(18)] typically have yields on the order of 10^{-3} times the primary yields, so neutron noise is of order 10% of the true signal due to these particles.

F. Detection efficiency in practical applications

When contrast limits are adjusted so they don't exclude proton tracks of a given diameter, the accelerator data show that 100% detection efficiency is achieved for protons of the corresponding energy as long as the incident proton trajectory is normal to the surface of the CR-39. As shown in Sec. V D, 100% detection efficiency can also be obtained for alpha particles. In practice, there is an upper limit on the energies of particles that can be studied no matter what analysis techniques are used, because higher-energy particles have low values of dE/dx and result in tracks that are too small to be conveniently detected and characterized with an optical microscope (for protons, that energy is about 10 MeV).[45] In addition, the detection efficiency is zero for charged particles whose angle of incidence exceeds a critical value.[42,45]

It is often desirable to impose limits on track diameter, track contrast, and/or track eccentricity to minimize response to intrinsic noise and neutron noise, though this can result in a compromise in which the signal-to-noise level is improved but the detection efficiency is reduced. Eliminating tracks with diameters larger or smaller than those of interest for a given charged particle can lead to rejection of some intrinsic noise and neutron-generated noise without a decrease in detection efficiency. Eliminating tracks with low optical contrast can reduce intrinsic noise, but can also reduce the efficiency of detection of tracks from the particles under study if they are close to the low or high energy detection limits; Figure 12 shows detection efficiency as a function of proton energy for different contrast thresholds. Limiting eccentricity is useful because our experiments are all set up to ensure that particles under study have trajectories approximately normal to the CR-39 surface, generating circular tracks; many tracks due to intrinsic noise or debris are noncircular, and the same is true of some neutron-induced events (since recoil particles and reaction products which do not travel in the forward direction produce eccentric tracks). Thresholds for eccentric-

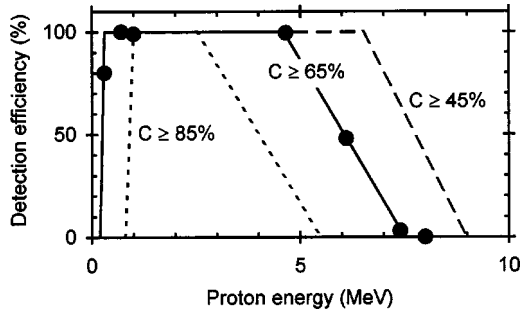

FIG. 12. Representative CR-39 detection efficiency for protons, as a function of energy, for different lower limits on the optical track contrast C. The data points are measurements for $C=65\%$, with data from the accelerator. The lines show approximate values for other energies and other values of C, based on data from OMEGA (these values can change significantly with changes in microscope optical adjustments and camera linearity). When noise is a problem, a contrast threshold of 65% is often chosen as a compromise between proton detection efficiency and noise rejection.

ity must be set to account for the small amount that results from not-quite-normal trajectories and for the eccentricity measured for the smallest tracks as a consequence of image digitization (as shown in Fig. 8). The best approach is to apply an eccentricity limit that varies with track diameter, being constant above some diameter limit (typically 8 or 10 μm) and then increasing as the diameter decreases.

In special circumstances where the thickness of the CR-39 is smaller than the range in CR-39 of the particle under study, another method can sometimes be used to minimize contributions of noise to data.[16] If the energies of the particle at impact on the front and on leaving the reverse both fall into the range of detection sensitivity, then there should be discernable tracks on both surfaces which line up with the trajectory of the particle. Intrinsic noise should be uncorrelated on the two surfaces, and neutron-generated noise should be less correlated than the desired particle data because knock-on protons are distributed in angle. Counting only those tracks with counterparts on the reverse therefore improves the signal-to-noise ratio.

G. Anomalies

Anomalies in the proton-track diameter distribution have occasionally been observed, especially when CR-39 has been exposed to x rays and/or heat (when diameters are smaller than normal). Alteration of CR-39 characteristics by x rays is discussed in Ref. 58. Anomalously small track sizes have also been seen in a few rare cases when x rays were not present. These anomalies are not totally understood; they can often be compensated for in data analysis if corresponding size anomalies are observed for another particle species.

H. Summary

In summary, CR-39 can be an efficient detector of the charged particles of interest in ICF experiments. Due to the dependence of track diameter on particle energy, the track size distribution automatically provides some spectral information for protons, deuterons, and tritons. While the energies of interest for heavier ions fall within the range of sensitivity of CR-39, protons from many reactions have energies that are too high for direct detection. In these cases, it is necessary to use a filter in front of the CR-39 to reduce proton energy by a known amount. In the next sections we will see how the characteristics of CR-39 discussed here make possible a wide range of useful spectroscopic measurements.

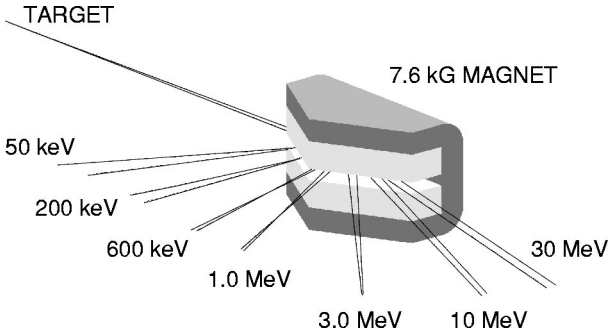

FIG. 13. Concept of the magnet-based CPSs, showing how the field of a 7.6 kG magnet separates protons of different energies. A proton or other charged particle passes through a collimating aperture (not shown) before entering the magnet, where its trajectory is determined by its gyroradius. After leaving the magnet, the particle is stopped in CR-39 (not shown). The magnets were fabricated by the Dexter Corporation (Ref. 59), and utilize magnetic material constructed of multiple pieces of Nd–Fe–B which are epoxied together. Steel pole faces smooth out inhomogeneities in the fields in the gap (where uniformity is ~2%), while a steel yoke and careful gap design result in minimal fringing fields (1000 and 250 G at 2 and 4 cm from the magnet edge, respectively). The size of the magnet was minimized to allow mounting in a re-entrant module inside the OMEGA target chamber; the longest dimension is 28 cm, the gap width is 2 cm, and the weight is 160 lb. The force between the poles is 6400 lb.

IV. SPECTROMETRY OF CHARGED PARTICLES FROM OMEGA USING CR-39

A. Magnet-based spectrometers

There are two magnet-based charged-particle spectrometers (CPSs) on OMEGA, each utilizing a 7.6 kG permanent magnet as shown in Fig. 13 and described in detail in the figure caption. After entering through an adjustable entrance aperture, each charged particle passes through the magnetic field along a trajectory determined by its gyroradius R_{gyro} before impacting particle detectors. The position at which it is detected can be characterized by R_{gyro} or by its square, which is proportional to the particle's energy E through the relationship

$$R_{\mathrm{gyro}}^2 \propto (A/Z^2)E, \tag{21}$$

where A is the atomic mass, and Z is the atomic number. If A and Z are known, the energy can be determined directly from the detection position. The magnet was designed for values of $(A/Z^2)E$ extending from 0.1 to 30 MeV, and protons, deuterons, tritons, ^{3}He, and alpha particles have been studied as we shall see. Special-purpose magnet-based spectrometers with more limited ranges of application have been used previously for 3.5 MeV DT alpha particles (using LR115 cellulose nitrate track detectors),[2] for protons from an intense proton beam (using CR-39 and pin diodes),[14] and for 3 MeV DD protons (using CR-39 detectors).[25]

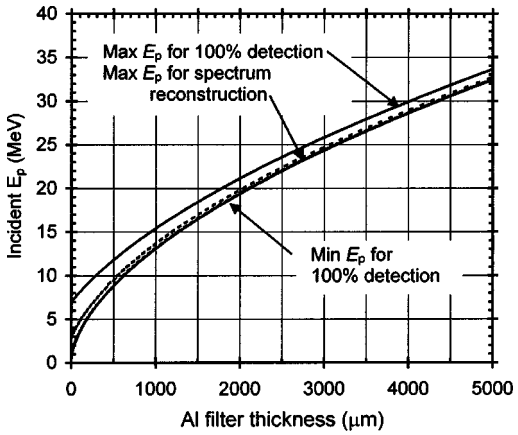

FIG. 14. The solid lines show, for a given filter thickness, the energies of protons that can be ranged down to the highest and lowest energies detectable by CR-39 with 100% efficiency. The broken lines show the energies of protons that will be ranged down to the highest and lowest energies useful for spectral measurements by CR-39. (The effects of energy straggling have been ignored.)

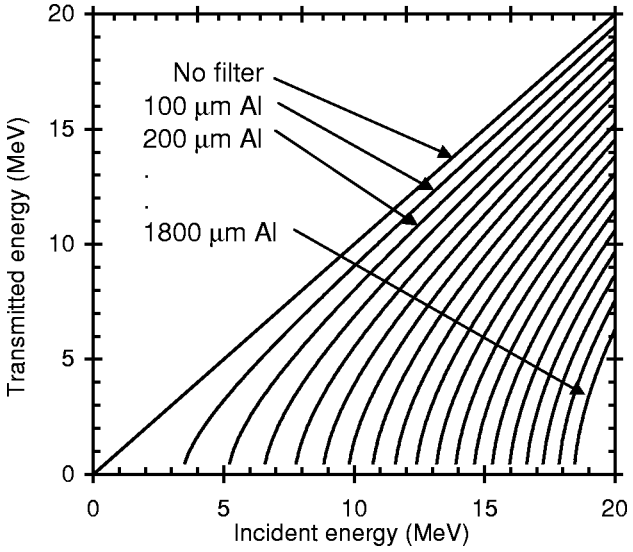

FIG. 15. The relationship between a proton's energies before and after passing through aluminum filters of different thicknesses. The values plotted here were generated using the program SRIM (Refs. 54 and 55), and ignore energy straggling.

The original concept for the CPSs included the use of CR-39 detectors.[14] The first actual instrument was designed for use with electronic particle detectors,[27,39] but it was eventually implemented with CR-39 detectors when it became apparent that they offered advantages of detection efficiency, coverage of large areas, energy resolution, and immunity to electromagnetic transients.[29] Since CR-39 is 100% efficient only for detecting protons in the interval from about 0.5 to 6 MeV under typical etch and scan conditions, it is necessary to use a filter in front of the CR-39 to range down the energy of any proton whose energy exceeds 6 MeV. Figure 14 illustrates the energies that get ranged down to the interval of sensitivity by aluminum filters of different thicknesses.

As will be seen in Secs. V and VI, particles with the same gyroradius but different mass and/or charge produce different signatures in CR-39; this makes possible the simultaneous measurement of spectra of different particles even when their trajectories in a CPS overlap [as in the case of the 3 MeV protons, 3.6 MeV alphas, and 1 MeV tritons generated in a DT plasma through reactions (1) and (3)].

The dynamic range of the CPSs is determined by the size of the entrance aperture, the distance from the target, and the minimum and maximum number of particles per unit area that can be utilized on the CR-39. The entrance aperture is 15 mm long (in the direction transverse to the magnet dispersion) and has a width that can be varied from 1 to 10 mm, depending on expected flux levels, giving solid angles between 10^{-6} and 10^{-5} when placed 100 cm from the target. The instruments can then be used with yields from 10^7 per MeV to more than 10^{13} per MeV. The absolute energy calibration is accurate to about ± 0.02 MeV at 3 MeV and ± 0.1 MeV at 15 MeV.[31] The response function for a monoenergetic proton beam of a given energy is a square box whose width is determined by the width of the entrance aperture; with a 1 mm aperture, the box has a standard deviation about the mean energy of 0.013 MeV for 3 MeV protons and 0.19 MeV for 15 MeV protons.

B. Simple range-filter spectrometers

A piece of CR-39 can be combined with a fixed-thickness filter to form a "range-filter" (RF) assembly, which can be used in different ways to study protons or other charged particles. The first way involves the measurement of a particle yield in a narrow energy band by counting the number of tracks per unit area on the CR-39. Let E_i be the energy of protons incident on an aluminum filter of thickness t, and let E_c be the energy of the protons after transmission through the filter. The relationship between E_i, t, and E_c can be written

$$E_i = E_i(E_c, t), \tag{22}$$

and is shown graphically in Fig. 15. Protons with energy E_c at CR-39 can be efficiently detected in the interval from about $E_c = 0.5$ to 7 MeV, so the interval of energies E_i that can be detected is from $E_i(0.5\,\mathrm{MeV}, t)$ to $E_i(7\,\mathrm{MeV}, t)$. These limits are plotted in Fig. 14, showing that as t increases, the width of the detectable incident energy interval becomes smaller. If a single filter provides for efficient detection of all energies of interest and if no other particles will be detectable under the same circumstances, then a simple count of tracks provides a yield (as discussed for alphas in Ref. 9 and in Sec. IV).

For example, an aluminum filter 1100 μm thick provides a detection interval from about $E_i = 13.8$ to 16 MeV, which is usually wide enough to cover most of the width of a 14.7 MeV D^3He proton line from reaction (5). It is not wide enough to cover the 12.6–17.5 MeV birth-energy range of secondary protons from reaction (9), and it will miss most of the D^3He proton line if that line has lost energy while passing through the shell of an imploded capsule.

Spectral information with higher resolution is available through two other approaches. The approach adopted here uses the fact that the diameter of a proton track in CR-39 is directly related to the incident energy E_c of the proton. Theo-

retically, a proton spectrum could be reconstructed from a diameter histogram. But at the highest energies shown in Fig. 6, and also near the diameter peak, there would be significant energy uncertainties since a small error in diameter would translate into a large error in deduced energy. At the low-energy end it would also be necessary to use contrast information to discriminate between tracks with the same diameter on opposite sides of the diameter peak. Realistically, accurate spectrum reconstruction is typically limited to the interval $E_c \approx 1.5-3$ MeV, where we can write

$$E_c = E_c(D). \tag{23}$$

If N is the number of proton tracks per unit area having diameters between D and $D+dD$ behind a filter of thickness t, then N is also the number of protons per unit area in the incident spectrum between energies $E_i(E_c(D),t)$ and $E_i(E_c(D+dD),t)$. The width of the interval in E_i for which a spectrum can be reconstructed in this way is shown in Fig. 14. The widest interval that can be covered at 15 MeV is about 0.8 MeV. Another approach to spectrum reconstruction, using the relationship between a particle's energy and the depth of its track in CR-39, requires that particles strike CR-39 at an angle and has been used for alphas[60] and protons.[21]

Because of the limited interval of particle energies that can be accurately studied with a single filter thickness, it is natural in many applications to use a ''step'' filter with sections of different thickness. Small numbers of steps have been used, without calculating spectral structure within each step, for broadband spectral information in ICF experiments for deuterons and tritons[10,15] and for protons,[12,16,19,22,23] while up to 20 steps, with spectral decomposition within each step, have been used for more detailed proton spectra from the interaction of high-intensity, short-pulse lasers with solids.[61]

C. Wedge-range-filter spectrometers

A generalization of the step wedge leads us to a filter with continuously varying thickness, which has advantages for compactness and for data reduction. Combined with a piece of CR-39, as illustrated schematically in Fig. 16, this filter forms a wedge-range-filter (WRF) spectrometer. By using a wedge with an appropriate range of thicknesses, it is possible to make an accurate reconstruction of a proton spectrum over a wide interval of incident energies by applying the technique discussed in the last section. The range of thicknesses required for a given energy interval can be determined from Fig. 14. A group of WRF spectrometers has been fabricated and used for the study of protons from 8 to 18 MeV using aluminum wedges covering the thickness range 400–1800 μm over an active area of about 2 cm$\times$2 cm. Because it is occasionally found that the proton fluence (but not energy) varies with position, as described in Sec. VI A 2, the WRF design incorporates strips of uniform filter thickness just outside the wedge region. If the proton fluence is seen to vary significantly along a strip parallel to the wedge gradient, the variation can be quantified for use in correcting data taken behind the wedge; uncorrected, such

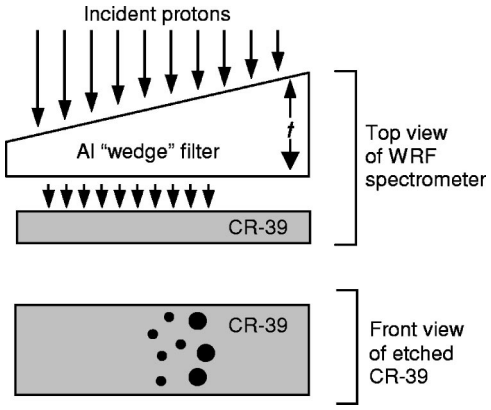

FIG. 16. Schematic illustration of a WRF proton spectrometer. The spectrometer itself consists primarily of a filter with a wedge-shaped cross section (thickness t varying along its length) and a sheet of CR-39. Some of the protons incident on the filter are energetic enough to pass through it, and they impinge on the CR-39, creating tracks of damage sites. After etching in NaOH, each of these tracks opens up into a hole at the surface with a diameter that depends on the proton energy (see Sec. III C and Fig. 6). A two-dimensional histogram of the number of tracks as a function of diameter and t can be converted into a histogram of protons per MeV in the incident proton spectrum.

variations can result in a small amount of distortion in the shape of an inferred spectrum, but very little error in the mean energy and no error in the energy endpoints.

In practice, the most difficult aspect of WRF implementation has been calibration. Filter fabrication with thickness errors under 5 μm is desirable, but has not been achieved thus far. In order to compensate for fabrication errors and for any errors in the theoretical model for proton energy loss in the filter, an end-to-end test and calibration for each filter was carried out with monoenergetic protons from the accelerator described in Sec. III. Deviations from ideal behavior were determined for each individual WRF and incorporated in data reduction algorithms. The current absolute measurement uncertainties (not including counting statistics) are about ± 0.1 MeV for energy and 12% for yield; future work with better fabrication accuracy should reduce these uncertainties. The response function of the WRFs to a monoenergetic, 13.8 MeV proton beam was measured to be roughly Gaussian, with a standard deviation of about 0.15 MeV; this is slightly larger than what would be expected due to the effects of energy straggling of the protons as they pass through the filter.

The WRF package is very compact, making it practical for fielding at many different locations during the same implosion, for symmetry studies; as many as eight have been used at one time. In addition, they can be placed relatively close to a target when the yield is expected to be low. Useful spectra have been measured for yields as low as 10^5/MeV, which is more than 2 orders of magnitude lower than the limit for the magnet-based spectrometers. They have also been used for yields as high as 10^{10}/MeV (this requires placement near the wall of the target chamber). They will not work for yields of 10^{11}/MeV or more, unless they can be moved well outside the OMEGA target chamber, because of track overlap in the CR-39. While they could be used for spectra of D or T, rather than protons, they are usually not

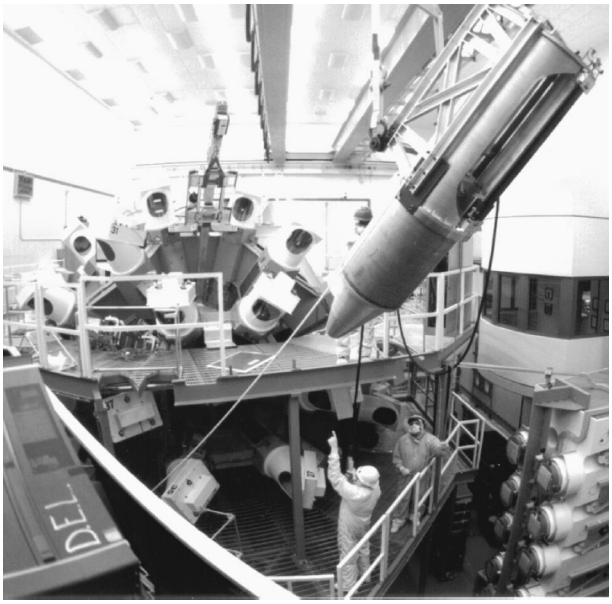

FIG. 17. The CPS2 spectrometer during installation on OMEGA flange H1 (see Fig. 18). The cone-shaped end contains the entry aperture, which is located 100 cm from the target position. Various materials are used in the structure for neutron shielding.

used for overlapping spectra of different particle types as the magnet-based spectrometers are; the CPSs can separate particles on the basis of both trajectory in a magnetic field and track diameter, while the WRFs as described here work only with track diameter and contrast and cannot always discriminate between different particle types with the same track diameter. Larger maximum WRF thicknesses will be used for protons of higher energy [e.g., the tertiary protons from Eq. (19)] in the future, but the present design has proven very useful for D ^{3}He p, secondary D ^{3}He p, and knock-on p. It has been brought to our attention that CR-39 and a wedge-shaped range filter have also been used in a different context to measure endpoint energies of proton spectra.[62]

V. SPECTRA FROM CAPSULE IMPLOSIONS AT OMEGA

A. Experimental setup

Figure 17 shows one of the CPSs being mounted on the OMEGA target chamber. Figure 18 illustrates the positions of diagnostic ports on OMEGA, and shows the mount positions of the CPSs and the locations of nine other ports which have been used for RF and WRF measurements (labeled TIM1–TIM6, and KO1–KO3). CPS1 and CPS2 have fixed capsule–detector distances of 235 and 100 cm, respectively, and are separated by 101° with respect to the capsule position. The RF and WRF detectors can be placed at distances from the capsule of 5–175 cm.

Other diagnostic instruments operate during capsule implosions, and of particular interest to us are the neutron diagnostics. Yields of primary neutrons are measured by Cu activation (for DT neutrons) and In activation (for DD neutrons). Yield-averaged ion temperatures are measured with a neutron time-of-flight (NTOF) diagnostic,[63] and secondary

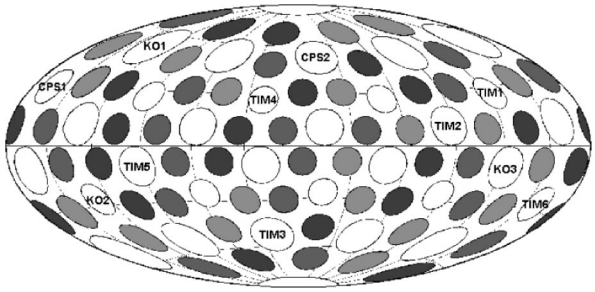

FIG. 18. Locations of ports on the OMEGA target chamber, shown on an Aitoff projection. The positions labeled CPS1 and CPS2 correspond to permanently-mounted, magnet-based spectrometers. The other labeled ports can sometimes be used for wedge-range-filter proton spectrometers.

neutron yields Y_{2n} are measured with a TOF diagnostic, Cu activation, or the MEDUSA[64] scintillator array.

Current OMEGA experiments utilize room-temperature capsules with fuel in gas form, and some cryogenic D_2 capsules. Since a major priority is development of techniques that will lead to high-performance cryogenic-capsule implosion, many experiments utilize room-temperature capsules with plastic shells from 15 to 24 μm thick and fuel pressures from 3 to 15 atm; these have predicted hydrodynamic properties relevant to those expected for cryogenic capsules.[65] The fuel composition is varied in these experiments, largely in order to obtain complementary diagnostic information. Thinner shells, and shells with different composition, are also occasionally used for special purposes.

We now look at data from a number of OMEGA implosions representing different fuel and shell types to clarify the principles of the spectrometers. All data correspond to experiments in which the laser pulse is 1 ns long, with nominally constant intensity; total laser energy varies, but is in the range from 12 to 24 kJ. Target capsule diameters are all in the vicinity of 900 μm, and the processing of CR-39 will be assumed to follow the procedures discussed in Sec. III B.

B. Spectra from an implosion with D^{3}He fuel

There are five charged primary fusion products from implosions of D^{3}He-filled capsules (see Table I). Only the 14.7 MeV proton can escape and be detected if a capsule shell is thick; it can be measured with either WRF spectrometers (if the yield is in the range of 10^5–10^{10}) or the magnet-based CPSs (if the yield is in the range of 10^7–10^{13}). If the shell is thin enough, four lower-energy products can also escape; they are always measured with the CPSs. This is illustrated in Fig. 19, which shows CPS2-measured spectra for five particle species from OMEGA implosion 20297. The capsule had 15 atm of D^{3}He fuel in a thin glass shell 2.5 μm thick. It was irradiated with 12 kJ of laser power in a 1 ns square pulse by 30 laser beams; the yield-averaged ion temperature was measured to be 9.5 keV, and the DD neutron yield was 2.3×10^{10}. The 14.7 MeV D ^{3}He protons and the 0.83 MeV DD ^{3}He have very different trajectories in the magnet than the other particles, and their spectra are measured simply by counting particle tracks as a function of position on the CR-39 (a filter is used just in front of the CR-39 to reduce the proton energies to the range of CR-39 sensitivity). The

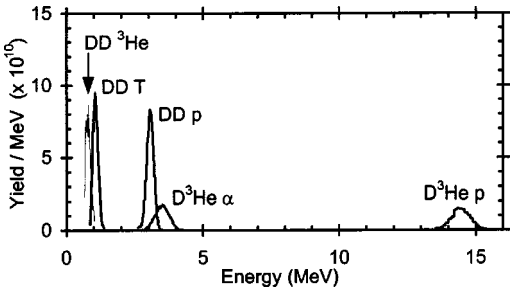

FIG. 19. CPS2-measured energy spectra of ^{3}He, tritons, and protons from DD reactions (1) and (2), and alphas and protons from D ^{3}He reaction (5), for OMEGA implosion 20 297 (D^{3}He fuel in a thin glass shell). The widths of such lines are affected by the temperature of the plasma, by differences in total pathlength in the fuel and shell plasma for the particles as they make their way out of the capsule, by the response function of the spectrometer, and sometimes by time evolution.

~3 MeV DD protons, ~1 MeV DD tritons, and ~3.6-MeV D ^{3}He alphas all have nearly the same gyro radius in the magnetic field, so they appear at about the same position at the detector plane of the CPS (and they overlap in position, because of the finite width of the lines). Since the diameters of the tracks are different for the three particles, they can be counted separately for measurement of their respective spectra. This is illustrated in Fig. 20, which shows the tracks at one particular position, and Fig. 21, which shows how the track diameters remain separate at all positions.

For each line it is possible to measure a mean energy, a linewidth, and a yield. The yields of the DD and D ^{3}He proton lines, which will be referred to in Sec. VI, are 2.7×10^{10} and 1.3×10^{10}, respectively. We note that CR-39 detection efficiency of about 1.1×10^{-4} for DD neutrons was mentioned in Sec. III. Since the fluxes of DD neutrons and D^{3}He protons are comparable, a signal-to-background ratio (S/B) of about 10^4 is obtained for spectra of the protons. Intrinsic noise is also negligible in this case, and the noise levels in the measured spectra are dominated strictly by counting statistics.

C. Spectra from an implosion with D_2 fuel

The previous subsection included spectra of DD protons, tritons, and ^{3}He from reactions (1) and (2) in capsules with D^{3}He fuel. The same reactions occur when the fuel consists only of D, and the same spectra can be measured as long as the shell is thin enough for a given particle to escape. The other charged-particle spectrum that is important for D_2 implosions is that of secondary protons from reaction (9), which are important for measuring fuel and shell $\langle\rho R\rangle$ as discussed in Sec. VI. This spectrum can be measured with either WRF spectrometers (if the proton yield is in the range 10^6-10^{10}) or the magnet-based CPS2 (if the proton yield is in the range 10^8-10^{13}).

OMEGA implosion 21210 involved 15 atm of D_2 fuel in a 24.1-μm-thick CH shell, and 23.5 kJ of laser light applied with 60 beams in a 1 ns square laser pulse. The ion temperature was measured to be 2.7 keV, while the yields of primary DD neutrons and secondary DT neutrons were 6.4×10^{10} and 1.3×10^8, respectively. Since secondary-proton yields are of order 10^{-3} relative to primary DD neutrons, while CR-39

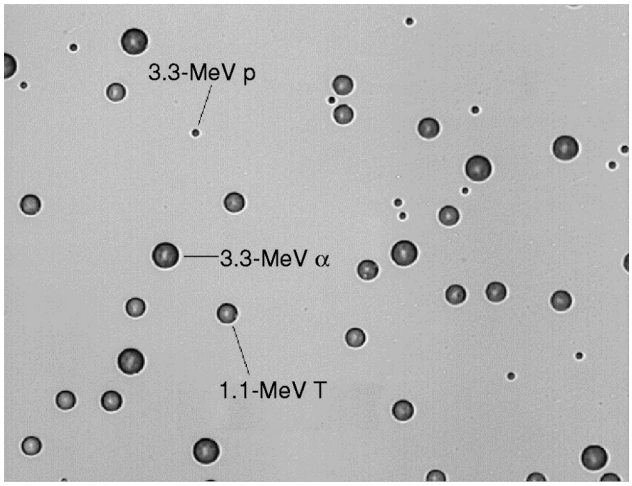

FIG. 20. Microscope image of CR-39 used in CPS2 for OMEGA implosion 20 297, with particle tracks produced by DD protons, DD tritons, and D ^{3}He alphas. The three particle types appear at this ''triple degeneracy'' point in the detector plane of the spectrometer because they have the same gyroradius in the magnet. Each particle type can easily be distinguished based on track size, as indicated in Fig. 21.

response to the neutrons is of order 10^{-4}, the signal-to-background level for WRF measurements is usually S/B~5–10. The relatively low flux levels make it desirable to place the WRFs fairly close to the capsules (15 cm in this case). Figure 22 shows a WRF-measured spectrum for which the mean proton energy was 12.9 MeV and the total yield was 7.6×10^7 protons.

D. Spectra from implosions with DT fuel

The most-used spectra from DT implosions are those of knock-on D and T from the fuel [reactions (12) and (13)], which are measured with the CPSs, and knock-on *p* from the shell [reaction (11)], which can be measured with either CPS or WRF.[33] In the CPSs, the D, T, and *p* have overlapping trajectories like the primary products of D^{3}He implosions described above in Sec. V B. Figure 23 shows a simple example of how track diameters differentiate the particles and

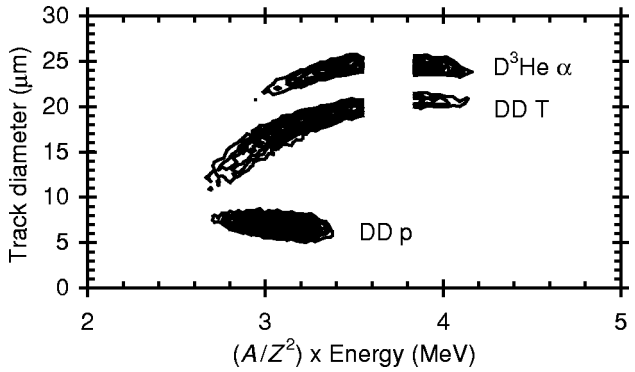

FIG. 21. A contour plot of the number of DD protons, DD tritons, and D ^{3}He alphas detected in CPS2 as a function of detection position [parameterized by particle energy according to Eq. (21)], for OMEGA implosion 20 297 (see Figs. 19 and 20). The energy gaps are due to a small physical gap in coverage between two adjacent pieces of CR-39. The particle species can be identified and separated on the basis of track diameters. The CR-39 was covered by an aluminum filter 6 μm thick.

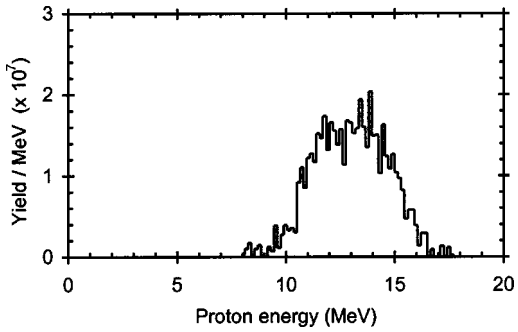

FIG. 22. WRF spectrometer measured spectrum of secondary protons from OMEGA implosion 21 210 (15 atm D_2 fuel in a 24.1 μm CH shell 972 μm in diameter; a 1 ns square laser pulse with 24.1 kJ of on-target energy; a measured T_i of 2.7 keV and a DD n yield of 6.46×10^{10}). The secondary protons have a yield of 7.6×10^7 and a mean energy of 13.0 MeV. Compare with Fig. 2.

allow them to be studied separately. A filter of one thickness was used over the entire CR-39 area in this case, making it particularly easy to see the continuous variations of track diameter versus energy for each particle. Separation of the particles on the basis of diameter, and subtraction of appropriate background levels, are involved in converting these data to spectra. In most situations a more complicated filter is now used, with thickness varying with position to make possible the coverage of a wider energy range for more particles on one piece of CR-39. CPS2- and WRF-measured spectra of the three knock-on particles from a more recent OMEGA implosion, number 23 445, are shown in Fig. 24. In this case the capsule contained 15 atm of DT gas in a CH shell 18.9 μm thick, and was irradiated with a 1 ns, 23.2 kJ pulse of laser light from 60 beams. The parameters of these spectra and their physical significance will be discussed in Sec. VI.

The CPSs can also be used to measure spectra of primary DT alphas from reaction (3); an example will be shown below for a DT^3He implosion. Another way to measure the yield of these alphas involves a simple RF detector consisting of CR-39 covered by a 6 μm Al filter. The number of tracks per unit area, multiplied by the area of a sphere with the radius of the detector, gives the total yield. This technique was recently used to cross-calibrate the detection of alphas by CR-39 with the measurement of DT–neutron yields by Cu activation and by MEDUSA. Since the alphas and neutrons come from the same reaction (3), their yields should be identical. Data were taken during three low-yield implosions of DT-filled capsules with 3.7-μm-thick CH shells and low fill pressures (0.04, 0.001, and 0.001 atm), irradiated by low laser energy (5 kJ in 30 beams twice, and 10 kJ in 60 beams once). The alphas were detected by CPS1, CPS2, and eight RF detectors located 20 cm from the capsules at different port locations (see Fig. 18). The results are shown in Fig. 25. Data from implosion 19 684 illustrate excellent agreement between yields measured with Cu activation $[(6.02\pm0.23)\times10^8]$ and with charged-particle measurements [on average $(6.0\pm0.2)\times10^8$]. In the data from implosions 19 685 and 19 686, the ratio of average RF-measured alpha yield to average MEDUSA-measured neutron yield was 1.11 ± 0.12, indicating statistical compatibility between these diagnostics. The conclusion drawn from these measurements is that the three different methods of measuring DT yields are consistent with each other, while the CR-39 efficiency is 100% for detecting the alphas. It is also notable that there are spatial variations within the measured charged-particle yields for each implosion (e.g., ~13% about the mean for implosion 19 684); this will be discussed in Sec. VI A.

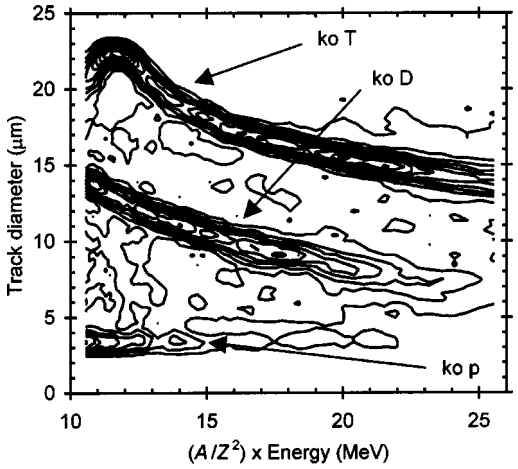

FIG. 23. Contours of the number of detected tritons, deuterons, and protons as a function of detection position (parameterized by energy) and track diameter in CPS2, for OMEGA implosion 13 817 (DT fuel in a shell consisting of 2.4 μm of glass and 5 μm of CH). A 50 μm aluminum filter covered the CR-39, and the particle species can readily be identified and separated on the basis of track size.

E. Spectra from implosions with more complicated fuels

Implosions of capsules with more exotic fuel and/or shell structure have also been performed. Figure 26 illustrates spectra of four fusion lines from an implosion involving DT^3He fuel. This is of interest primarily as another illustration of the simultaneous measurement of multiple spectra and as an example of the T^3He deuteron line. Implosions of capsules with DTH fuel in glass shells[20] or pure CD shells[34] have recently provided spectra of proton knock-ons from the fuel, which make possible the study of fuel $\langle\rho R\rangle$ (as described in Sec. VI B for knock-on deuterons and protons). Data from multiple WRF spectrometers were used in Ref. 36 to study shell symmetry. Other types of capsules with multilayer shells have been used to determine the degree of interpenetration of fuel and shell (see Sec. VI E and Refs. 66–69 and 37).

F. "Ablator" ions

Fast protons from the shell, accelerated to energies up to 1.4 MeV by electrostatic fields in the laser–plasma interaction region (see Sec. VI A) are observed in large numbers at laser intensities of $\sim10^{15}$ W/cm^2.[32] Such maximum proton energies are much higher than would be expected from comparisons with other laser experiments performed at the same $I\lambda^2$, where I is the laser intensity and λ is the laser wavelength. In addition to protons, heavier fast ions, such as carbon, have also been observed, though quantitative analysis is complicated by the difficulty in identifying the multiple

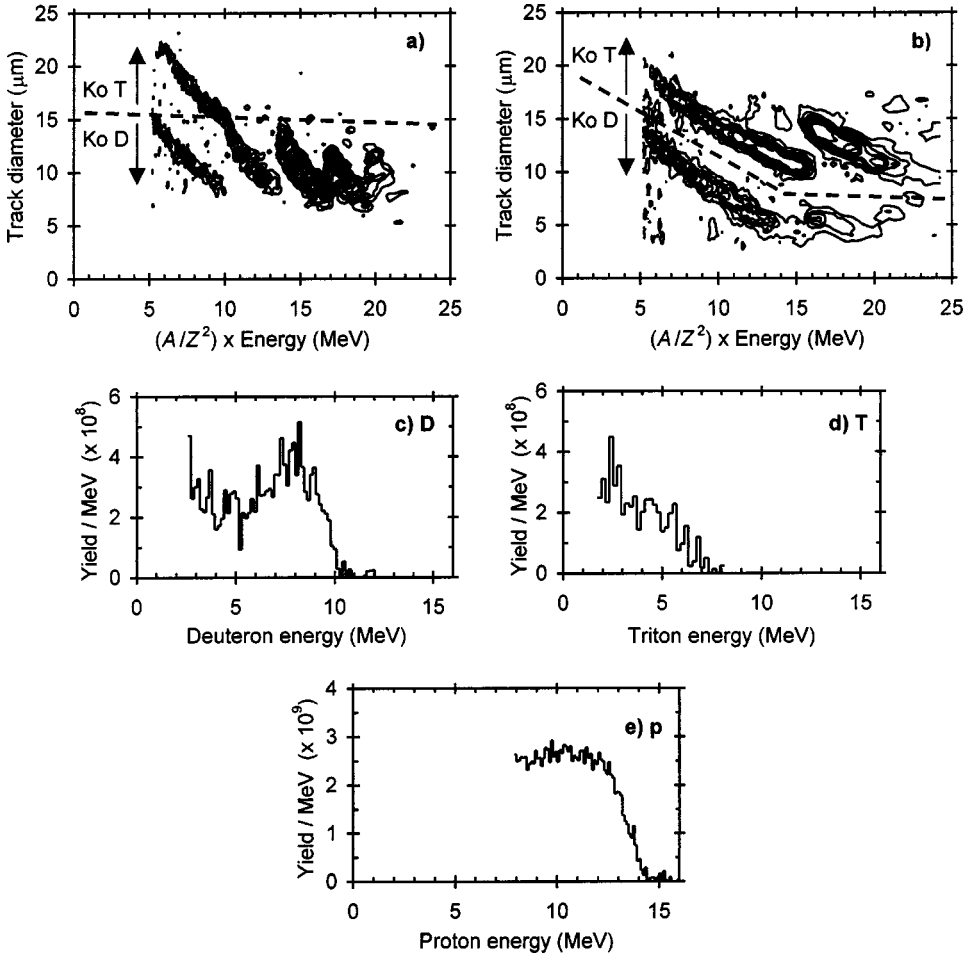

FIG. 24. Knock-on data from OMEGA implosion 23 445 (15 atm DT fuel in a 18.9 μm CH shell 932 μm in diameter; a 1 ns square laser pulse with 23.2 kJ of on-target energy; a measured T_i of 4.1 keV and a DT n yield of 1.95×10^{13}). Plots (a) and (b) illustrate the nature of raw data from CPS2, showing contours of the number of tracks vs. track diameter and detection position parameterized by particle energy. The filter covering the CR-39 was made in several segments to optimize the detectability of the desired particle over a wide energy range. In (a) there are five different filter thicknesses, and the deuteron diameter can be seen to change at each filter boundary. In (b), there are two filter thicknesses. The knock-on D spectrum (c) was calculated from the D data illustrated in (a), and the yield (as defined in the caption of Fig. 3) is 1.5×10^{9}. The knock-on T spectrum (d) was calculated from the T data illustrated in (b); a yield cannot be measured because of the distortion in shape caused by a large energy downshift relative to the birth spectrum. The knock-on proton spectrum shown in (e) was calculated from WRF data; the yield per MeV in the flat region is 2.6×10^{9}.

charge states. The proton spectra sometimes show distinctive, regular line features, as illustrated in Fig. 27; the precise mechanism behind the generation of these lines is not understood, but it is possible that they are associated with ion acoustic perturbations in the plasma. Another theory is based on a periodically discharging target releasing particles at decreasing energies.[70]

VI. DIAGNOSTIC USE OF CHARGED-PARTICLE SPECTRA

To put the methods described here in a better physical context, and to point out important issues affecting their use and interpretation, this section provides a brief overview of some of the ways they are actually used, citing data from Sec. V and other publications for examples. For simplicity, measurement uncertainties are ignored and references to other papers are given for more details of analysis and interpretation. The discussion is divided according to physical regions. Conditions outside the imploded capsules (Sec. VI A) can sometimes affect the charged particles during their passage from capsule to detector and have an impact on analyses of charged-particle data. The fuel material (Sec. VI B) and shell material (Sec. VI C) in compressed capsules are considered separately, although it is likely that there is a region in which the two are actually mixed together as a consequence of instabilities at the interface (Sec. VI E). Capsule symmetry is discussed in Sec. VI F. All measurements illustrated here correspond to time averages. Most fusion products are generated during a fairly short (~150 ps) burn interval, while ions from the shell coming from laser–plasma interactions are generated during the laser pulse (~1 ns long). As mentioned below (Sec. VI A), the burn interval may occur during or after the laser pulse, depending on the capsule type and laser conditions.

A. Conditions outside the compressed capsule

1. Particle energy modification through electrostatic acceleration

Charged-particle measurements have demonstrated that the energies of particles from certain types of implosions exceed their theoretical birth energies by 0.5 MeV or more[4,5,17,29,30,32] (see Fig. 26). Laser–plasma interactions in the target corona result in the escape of hot electrons from the target, charging the capsule to a positive potential and accelerating positively charged ions leaving the capsule. The potential is peaked near the beginning of the laser pulse and decays steadily thereafter;[6,11] it is negligible by a few hundred ps after the termination of an OMEGA laser pulse, as demonstrated in a series of experiments[33] involving measurement of many spectra of knock-on protons from the 20-μm-thick CH shells of DT-filled capsules imploded at OMEGA with 1 ns laser pulses. The protons, which in these experiments are generated 300–600 ps after completion of the laser pulse, were found to have a high-energy endpoint at the

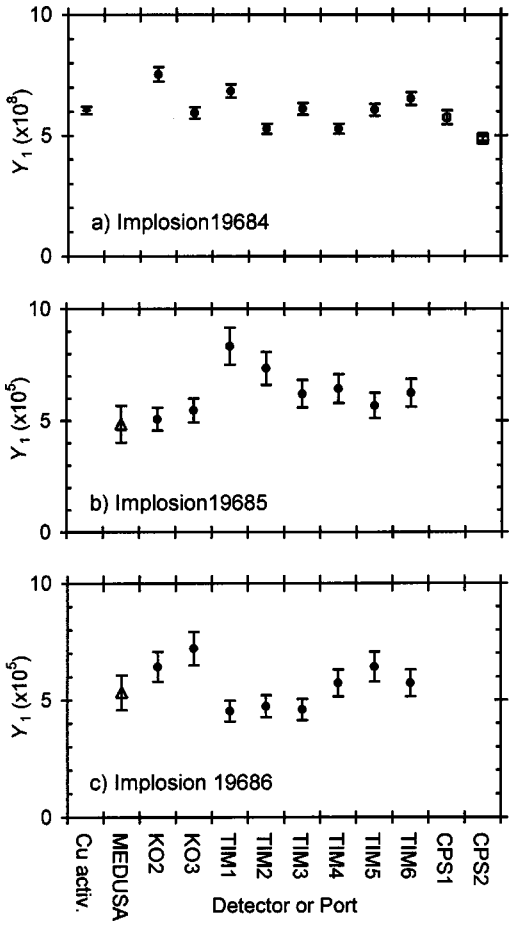

FIG. 25. (a) Primary yields for three OMEGA implosions. The neutron yield was measured with either thick Cu activation or by the MEDUSA neutron spectrometer, while the alpha yields were measured by CR-39-based rf detectors at the ports K02–TIM6 and (for implosion 19 684) by CPS1 and CPS2. The scatter in the yields of alpha particles within individual implosions is discussed.

birth-spectrum limit of 14.1 MeV to within experimental uncertainties [see Fig. 24(e)]. Since the endpoint energy corresponds to protons scattered at the surface of the shell, there is no energy loss due to interactions with the shell plasma; if there were any acceleration it would be observed directly as an increase in this energy.

Whether charged fusion products are accelerated therefore depends on whether the burn interval occurs during the laser pulse, as it tends to for implosion of thin-shell capsules, or after the laser pulse, as it does for implosions of capsules with thick shells (such as 20 μm of CH). The measured energy of any charged fusion product is determined by its birth energy, by any acceleration it experiences, and by the slowing down it experiences due to interactions with the fuel and shell plasma. In the case of thin-shell capsules, simultaneous data from several particles can sometimes be used to separate the contributions of acceleration and slowing down, as discussed in Sec. VI G. In the case of thick-shell capsules, acceleration can generally be ignored and all modification of particle energy can be attributed to energy losses due to slowing in the plasma. This is important for the analyses described below.

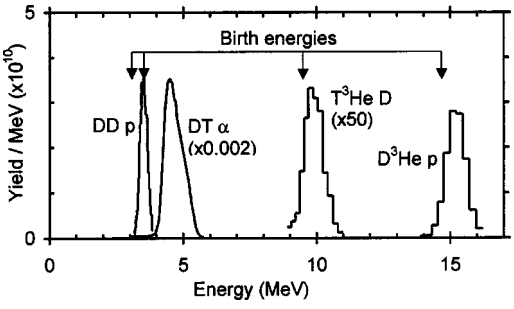

FIG. 26. CPS2-measured spectra from OMEGA implosion 14 972 (D–T–^{3}He fuel in a thin glass capsule). The lines are all upshifted relative to their birth energies because the burn time occured during the laser pulse. Note that the upshift for the DT α is twice that of the other particles because it has twice the charge.

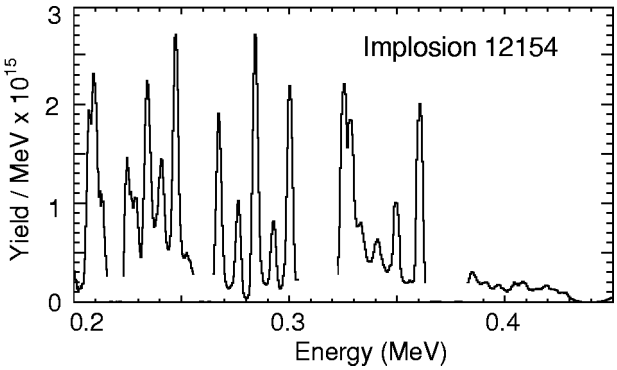

FIG. 27. Spectrum of ablator protons from OMEGA implosion 12 154, measured with CPS1. In this case the yields were high; a short CR-39 etch time (~10 min) was used to make the track diameters small in order to avoid overlap, and high magnification (×100 objective) was used to count the small tracks that resulted.

2. Possible modification of locally measured yields

As shown in Fig. 25, it is sometimes found that different yields are measured at different angles with respect to a capsule during the same implosion. This effect has also been noted for measurements of secondary protons[22,34] and discussed in more detail for other scenarios in Ref. 35. When measurements display such spatial variations, they typically have a distribution of values with standard deviation of order 20% about the mean. Although spatial variations in energy are sometimes seen (as discussed in Sec. VI C), they are generally not correlated with yield variations. In fact, measurements that show yield variations very often accompanied by no energy variations, leading us to believe that the yield variations probably do not result from structure in the capsule. Something is changing particles' directions without changing their energies; while a complete explanation is lacking, two possibilities are small azimuthal electric fields or magnetic fields outside the capsules.[25,35] Regardless of the mechanism behind the variations, they indicate that any yield inferred from a single detector measurement may deviate from the total yield over 4π steradians, and that the uncertainty may be of order 20%. Simultaneous measurements at different positions, with different detectors, reduces this uncertainty. Until the explicit discussion of asymmetries, below, we will ignore them for simplicity.

TABLE II. Values of the coefficients B_{21} used in Eq. (24).[a]

Secondary product	B_{21}
Knock-on D[b]	8.0×10^4 mg/cm^2
Knock-on T[b]	5.9×10^4 mg/cm^2
Secondary D ^{3}He p[c]	5.2×10^3 mg/cm^2 ($\pm$10%)

[a]Derived from Refs. 33 and 34.
[b]For implosions of capsules containing fuel with equal number densities of D and T, and yields defined as described in the caption of Fig. 3.
[c]For implosions of capsules containing D_2 fuel, and subject to the limitations described in the text. This value is accurate for plasma electron temperatures up to about 10 keV and for values of $\langle\rho L\rangle$ below saturation. The "$\pm$10%" represents the fact that B_{21} varies slightly with $\langle\rho L\rangle$ and slightly with plasma temperature, as shown in Fig. 28.

B. The compressed fuel

1. Primary fusion yields

Yields of primary fusion reactions provide one of the most fundamental indicators of implosion performance, and measurements of primary neutron yields have traditionally performed this function. When charged fusion products are energetic enough to escape the shell and be measured, their yields provide an alternative to measured neutron yields. When yields of more than one primary reaction can be measured separately, it is sometimes possible to use them to estimate the fuel temperature, as described below.

2. Areal density

The fuel areal density $\langle\rho R\rangle$ at burn time, the integral of $\rho(r)\mathrm{d}r$ from $r=0$ to the outer boundary of the fuel, provides an important measure of radial compression. Two methods of estimating $\langle\rho R\rangle_{\mathrm{fuel}}$ from charged-particle measurements rely on the same basic principle: An energetic primary fusion product interacts with the thermal fuel to produce a secondary product; the ratio of the secondary yield (Y_2) to the primary yield (Y_1) is proportional to the number of fuel "targets" encountered by the primary product, and this is related to the areal density. The "knock-on" method applies to DT implosions, where the primary product is the 14.1 MeV DT neutron from reaction (3) and the secondary product is either the elastically scattered knock-on D or the knock-on T from reactions (12) and (13).[7,10,15,20,33] The "secondary-proton" method applies to D_2 implosions, where the primary product is the ^{3}He from DD reaction (2) and the secondary product is the D ^{3}He proton from reaction (9).[8,12,16,22,34] Both methods can be described through the equations

$$\langle\rho L\rangle_{\mathrm{fuel}}=B_{21}(Y_2/Y_1), \tag{24}$$

$$\langle\rho R\rangle_{\mathrm{fuel}}=A_{\mathrm{fRL}}\langle\rho L\rangle_{\mathrm{fuel}}, \tag{25}$$

where $\langle\rho L\rangle_{\mathrm{fuel}}$ is the mean path through the fuel for the primary fusion product, B_{21} is a coefficient shown in Table II and A_{fRL} is a geometric parameter close to 1 that depends on the radial distribution of the production of primaries within the fuel and the radial distribution of ρ. The shapes of these radial profiles are not usually known, although new methods of measuring them directly with charged-particle data[71] are showing promise. As a result, analyses are often performed with one of two simple models. In the "hot-spot" model of fuel structure, where the fuel is spatially uniform except that primaries come from an infinitesimal hot spot at the center, $A_{\mathrm{fRL}}=1.0$. In the "uniform" model of fuel structure, with primaries produced everywhere, $A_{\mathrm{fRL}}=1.33$.

A practical complication in the knock-on method is that it is hard to measure the yield if the spectrum is downshifted greatly, because distortion of the spectrum shape makes it difficult to isolate the equivalent of the high-energy peak in the birth spectrum [compare Figs. 3 and 24(d)]. A complication in the secondary-proton method is that DD ^{3}He slow down continuously due to normal interactions with the plasma until they either become thermalized or react with a deuteron *via* reaction (9). If they lose all of their energy before they leave the fuel, either because $\langle\rho R\rangle_{\mathrm{fuel}}$ is large or because the rate at which they lose energy is large (as when the temperature is low), the proportionality of the yield ratio to $\langle\rho L\rangle_{\mathrm{fuel}}$ is lost and a saturation occurs as shown in Fig. 28. For data in the saturated region, it is possible to determine only a lower limit on $\langle\rho L\rangle_{\mathrm{fuel}}$ with this method (although the saturated yield ratio can be used to estimate the fuel electron temperature if that temperature can be assumed uniform as discussed in Sec. VI B 5).[34] Making the saturation issue more important is the fact that the actual saturation limit may be lower than estimated from the yield-averaged ion temperature if the outer portion of the fuel is cold, as it may be if a large amount of shell material is mixed into the fuel.

As illustrations, we can apply Eqs. (24) and (25) to data from Sec. V for OMEGA implosions 23 445 and 21 210, using the parameters from spectra in Figs. 24(c) and 22. For the knock-on deuteron data from DT implosion 23 445, $Y_2/Y_1=7.7\times10^{-5}$ and $\langle\rho L\rangle_{\mathrm{fuel}}=6$ mg/cm^2. This leads to $\langle\rho R\rangle_{\mathrm{fuel}}=6$ mg/cm^2 for the hot-spot model, or 8 mg/cm^2 for the uniform model. For DD implosion 21 210, the ratio $Y_2/Y_1=1.2\times10^{-3}$ is close to the saturation limit for the measured ion temperature of 2.7 keV (as shown in Fig. 28). We therefore find $\langle\rho L\rangle_{\mathrm{fuel}}$ graphically rather than with Eq. (24), to obtain 6 mg/cm^2 (hot-spot model) or 8 mg/cm^2 (uniform model). Corresponding values of $\langle\rho R\rangle_{\mathrm{fuel}}$ are 6 mg/cm^2 (hot-spot model) or 10 mg/cm^2 (uniform model), and they might be regarded as lower limits because of the proximity of the yield to the saturation limit.

The knock-on and secondary-proton methods have both been used in studies of how different laser conditions affect implosion performance,[33,34,67] where it was shown[33,34] that the knock-on method gives $\langle\rho R\rangle_{\mathrm{fuel}}$ values for DT-capsule implosions that are very similar to those obtained with the secondary-proton method for D_2-capsule implosions when laser conditions and capsules are similar and the only difference is in the fuel composition.

Another related method for estimating $\langle\rho R\rangle_{\mathrm{fuel}}$ in D_2 implosions involves measurement of the yield of secondary neutrons from reaction (10).[16,18] This method has the advantage that the yield ratio Y_2/Y_1 saturates at a higher value of $\langle\rho L\rangle_{\mathrm{fuel}}$ than the yield ratio for secondary protons, but the disadvantage that the relationship between the yield ratio and $\langle\rho L\rangle_{\mathrm{fuel}}$ is nonlinear and temperature sensitive even below the saturation region. Partly as a consequence of this temperature dependence, the secondary-neutron method often gives values of $\langle\rho L\rangle_{\mathrm{fuel}}$ somewhat higher (by up to a factor

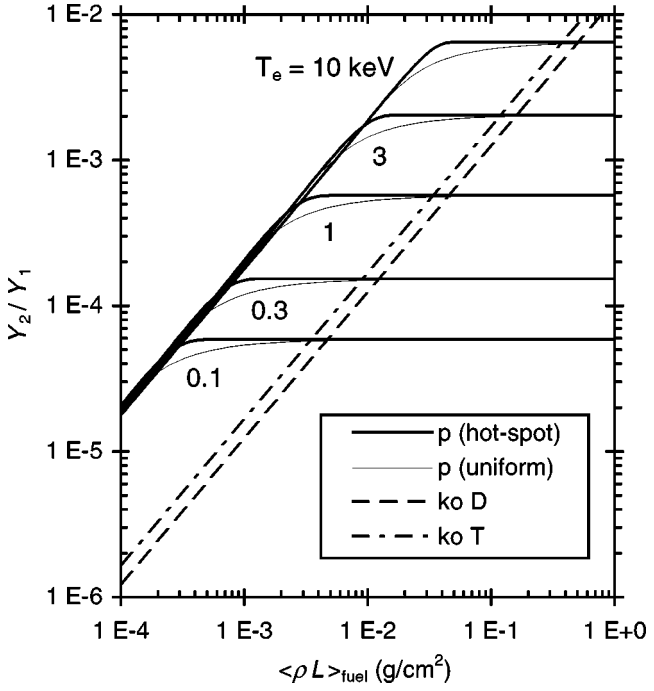

FIG. 28. Relationship of secondary yield (Y_2) to associated primary yield (Y_1) and the mean pathlength of primaries in the fuel ($\langle \rho L \rangle_{\text{fuel}}$) for reactions (9), (12), and (13). The curves for secondary protons, shown for both hot-spot and uniform models, are calculated as in Ref. 34 except that the temperature dependence of reaction (9) was included here (the difference is very small for temperatures $\leqslant$10 keV); a fuel density of 3 g/cm^3 was assumed, but the dependence on density is very weak and affects only the saturation levels. The electron temperatures labeling the different proton curves correspond to the bulk of the fuel volume in which the secondaries are generated; in the uniform model this is equivalent to the ion temperature measured by neutron diagnostics, but in the hot-spot model it can be lower. The curves for knock-on deuterons and tritons, taken from Ref. 33, are the same for the hot-spot and uniform models. They are also independent of temperature and density.

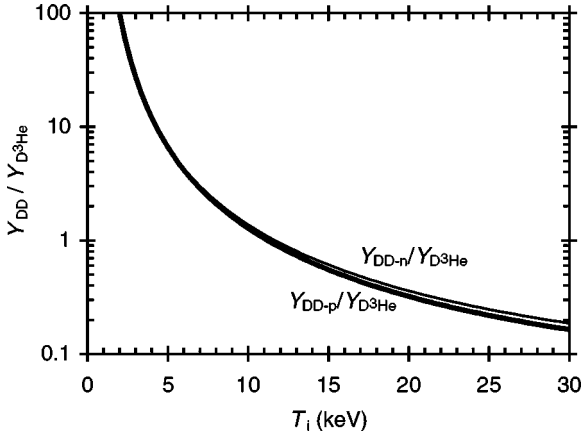

FIG. 29. The ratio of the DD neutron and proton yields to the D–^{3}He proton yield, plotted against ion temperature (from the rate coefficients in Fig. 1).

of 2) than those derived with the secondary-proton method.[34] This discrepancy may be exacerbated by the effects of fuel-shell mix, since it is known that the cooling of the outer region of the fuel due to mix can enhance the secondary neutron yield while diminishing the secondary proton yield.[22]

3. Radial compression

The radial compression ratio *CR* for a gas-filled capsule is defined as the ratio of the uncompressed fuel radius R_0 to the final fuel radius and can be written

$$CR = Q[\langle \rho R \rangle_{\text{fuel}} / \rho_0 R_0]^{1/2}, \tag{26}$$

where ρ_0 is the uncompressed mass density and the coefficient Q depends on $\rho(r)$ in the compressed fuel. The value of R_0 is known, and the value of ρ_0 can be calculated from the uncompressed fill pressure ($\rho_0 = a_f P_0$, where a_f in g cm^{-3} atm^{-1} is 2.24×10^{-4} for DT or D^{3}He fuel, and 1.79×10^{-4} for D_2 fuel). The value of Q is 1.0 for both uniform and hot-spot models ($d\rho/dr = 0$), but $Q > 1.0$ if $d\rho/dr > 0$ and $Q < 1.0$ if $d\rho/dr < 0$. For the implosions studied above, values of *CR* can be calculated if we assume $Q = 1$. The results are 6 or 7 (hot-spot or uniform model) for DT implosion 23 445, and 7 or 9 (hot-spot or uniform model) for D_2 implosion 21 210.

4. Ion temperature

One method for studying the fuel ion temperature T_i with line spectra of charged, primary fusion products is to determine the temperature necessary to explain the linewidths by thermal broadening. Reactions in a uniform, thermal plasma produce particle spectra whose shapes have the form $\exp[-(E-\langle E \rangle)^2/2\sigma^2]$; the ion temperature is related to the Doppler width σ through the expression $T_i = \sigma^2/C$, where T_i and σ are both in keV and C is 5880 for D^{3}He products, 5630 for DT products, and 1510 for DD-*p* and DD-T.[29] Early attempts were made to apply this method with the DT-α spectral line from thin-shell capsules, as measured with a scintillator-based TOF diagnostic,[1,6] but the result was thought to represent an upper limit on T_i because there are other sources of line broadening (which could include different pathlengths through the shell, time-varying acceleration, or ρR time evolution). Similar problems were found for D^{3}He protons.[33] Attempts have also been made with DD protons.[21,24]

Another method makes use of the fact that, if products of more than one reaction can be detected simultaneously, the possibility exists for comparing the ratio of their yields to the ratio of the theoretical rates for the reactions. Since these rate ratios often vary with ion temperature (see Figs. 1 and 29), yield measurements can be used to estimate a yield-averaged fuel ion temperature. This has been done with TOF spectral measurements of DT-α and DD-*p* yields from DT plasmas,[6] and more recently with CPS measurements of DD-*p* and D^{3}He-*p* yields from D^{3}He plasmas.[33] As an example, the ratio $Y_{\text{DD-}p}/Y_{\text{D}^3\text{He}}$ from the spectra shown in Fig. 19 implies (by way of Fig. 29) an ion temperature of 8 keV; the ratio $Y_{\text{DD-}n}/Y_{\text{D}^3\text{He}}$ (using the neutron yield measured with the NTOF diagnostic) implies $T_i \cong 9$ keV. These can be compared with the temperature of 9.5 keV that was measured with NTOF, and the agreement is reasonable. Figure 30 shows similar data from a wide range of implosions, demon-

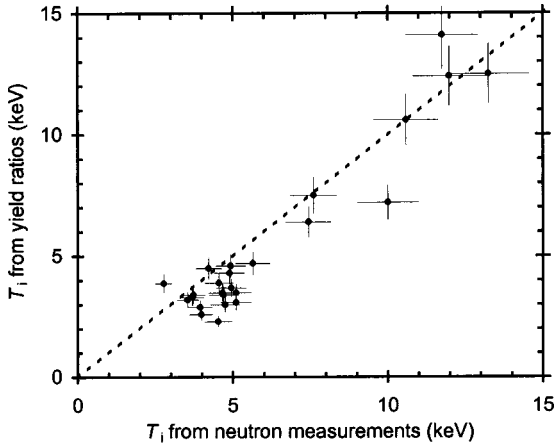

FIG. 30. Ion temperatures measured by using the ratio of DD neutron yield to D ^{3}He proton yield, plotted against ion temperature determined by the neutron time-of-flight spectrometer, for OMEGA D^{3}He implosions (Ref. 30).

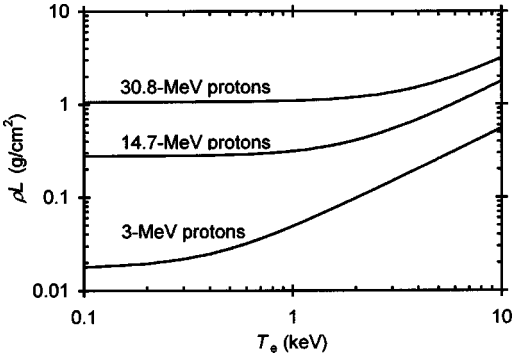

FIG. 31. The range of protons with important energies in a CH plasma for a variety of electron temperatures (at a density of 20 g/cm^3); results for a D plasma are nearly identical. The 3.0 and 14.7 MeV protons from reactions (1) and (5), and secondary protons with similar energies from reaction (9), are useful for probing current experiments, while the highly-penetrating 30.8 MeV proton from tertiary reaction (19) could be useful under future, high-density conditions.

strating reasonable agreement between charged-particle-derived temperatures and neutron-derived temperatures over a substantial range of temperature.

5. Electron temperature

As mentioned above, secondary protons from implosions of D_2-filled capsules have the characteristic that the ratio of their yield to the yield of primary DD neutrons is a linear function of $\langle \rho R \rangle_{\text{fuel}}$, but that for a given fuel temperature there is a maximum value of this yield ratio (see Fig. 28 and Ref. 34). While this limits the regime in which secondary-proton yields provide direct information about $\langle \rho R \rangle_{\text{fuel}}$, it opens up the possibility of using the yield to estimate the mean fuel electron temperature if the yield is known to be saturated and the fuel temperature can be assumed to be uniform.

C. Shell areal density

Part of the shell is ablated away during laser exposure. The areal density $\langle \rho R \rangle_{\text{shell}}$ of the remainder is the integral of $\rho(r)dr$ from the inner boundary of the shell to the outer boundary, and it can be studied with two basic methods using charged particles. The first method involves inferring $\langle \rho R \rangle_{\text{shell}}$ from the energy lost by particles of known birth energy due to slowing in the shell (Fig. 31 illustrates the values of $\langle \rho R \rangle$ for which protons of three important energies could escape and be detected). The second method involves measuring the fraction of primary neutrons that produce knock-on protons from the shell, which is proportional to $\langle \rho R \rangle_{\text{shell}}$. With both methods, the quantity directly inferred is the mean path through the shell for the charged particles or neutrons from the fuel, or $\langle \rho L \rangle_{\text{shell}}$. The ratio $A_{\text{sRL}} \equiv \langle \rho R \rangle_{\text{shell}} / \langle \rho L \rangle_{\text{shell}}$ is 1 in the limiting case of the hot-spot fuel model, and smaller than 1 in all other cases by an amount that depends on the ratio of shell thickness to shell radius and on the radial distribution of charged-particle generation in the fuel (see Fig. 32).

The energy-loss method requires the absence of acceleration effects and the use of a theoretical formalism such as that of Ref. 72 to relate $dE/d\langle \rho L \rangle$ to plasma parameters (it can vary with plasma density, electron temperature T_e, and chemical composition). Such measurements have been attempted using DD protons;[21,25] using DD protons and DT alphas;[6,11,13] and using DD tritons, DD protons, D ^{3}He alphas, and D ^{3}He protons.[31] The difficulty with using the low-energy particles is that $dE/d\langle \rho L \rangle$ is sensitive to T_e (as shown in Fig. 33) because the particle velocities are comparable to plasma electron velocities. This problem was solved in Refs. 6, 11, 13, and 31 by using downshifts of different particles to determine self-consistent values of T_e and $\langle \rho L \rangle$. These measurements can also be distorted by acceleration, which is often present for thin-shell capsules; spectra of at least three particle types are then necessary for $\langle \rho L \rangle$ determination.[31] For thick-shell capsules of the type under consideration here, the acceleration problem disappears and single energy loss measurements of protons with energies $\sim$15 MeV can be used because their velocities are high enough to make $dE/d\langle \rho L \rangle$ independent of shell T_e for typical shell T_e (see Fig. 33) and also insensitive to density and

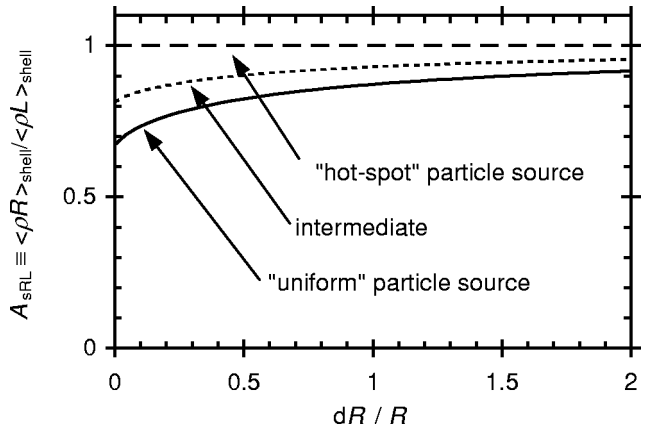

FIG. 32. The ratio of radial pathlength through a shell to the mean pathlength for particles originating in the volume inside the shell. R is the inner shell radius and dR is the shell thickness. If the source of particles under study is centrally peaked, the ratio $\langle \rho R \rangle / \langle \rho L \rangle$ is always 1; otherwise the ratio is less than 1. The curve labeled ''intermediate'' corresponds to a constant number of source particles per unit radius, while the curve labeled ''uniform'' corresponds to a constant number of source particles per unit volume.

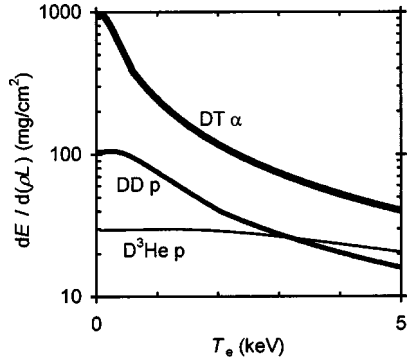

FIG. 33. Slowing down rates for three different particles in a CH plasma at density 20 g/cm^3, plotted as a function of plasma electron temperature, showing how rates for 3.5 MeV alphas and 3 MeV protons are quite sensitive to T_e while those for 14.7 MeV protons are relatively insensitive to T_e.

chemical composition (Fig. 34); this means that uncertainties in these parameters do not introduce large errors in inferred values of $\langle \rho R \rangle_{\text{shell}}$.

In the case of thick-shell capsules with D^{3}He fuel, the energy loss of primary 14.7 MeV protons has been used to estimate $\langle \rho R \rangle_{\text{shell}}$ as discussed in detail in Ref. 30. For thick-shell capsules with D_2 fuel, secondary protons can be used.[34] As an example, we can look again at data from implosion 21 210 (Fig. 23). The mean proton energy was 13.0 MeV, while the mean birth energy was 15.0 MeV, so the mean energy loss was 2.0 MeV and must be accounted for by losses in the fuel and losses in the shell. Since the radial profiles of the plasma parameters are not known, implications of the two different models discussed in Sec. VI B 2 will be found with results for the hot-spot model quoted first and results for the uniform model given in brackets. Energy losses in the fuel can be estimated from $\langle \rho R \rangle_{\text{fuel}} = 6[10]$ mg/cm^2 (found in Sec. VI B 2). In the hot-spot model, where primary ^{3}He are produced only at the fuel center, secondary protons are produced throughout the fuel with approximately equal numbers per unit radius and the mean pathlength traveled in the fuel is $\langle \rho L \rangle_{\text{fuel}} \cong 0.87 \langle \rho R \rangle_{\text{fuel}}$. [In the uniform model, where primary ^{3}He are produced everywhere, secondary protons are produced throughout the fuel with approximately equal numbers per unit volume and $\langle \rho L \rangle \cong 0.75 \langle \rho R \rangle_{\text{fuel}}$.] Using this value of $\langle \rho L \rangle_{\text{fuel}}$, together with a density inferred from the compression ratio *CR* (found in Sec. VI B 3) and an electron temperature assumed equal to the measured ion temperature, we can estimate that the mean energy loss in the fuel is about 0.17 [0.23] MeV. The remaining 1.83 [1.77] MeV energy loss due to the shell implies $\langle \rho L \rangle_{\text{shell}} \approx 59$ [57] mg/cm^2 (assuming a 1 keV, 20 g/cm^3 CH plasma). To find $\langle \rho R \rangle_{\text{shell}}$ from Eq. (25), we need to find the appropriate value of A_{sRL}. Using the calculated value of *CR*, together with the assumptions listed above, we can determined from Fig. 32 that $A_{\text{sRL}} \approx 0.89$ [0.82] and $\langle \rho R \rangle_{\text{shell}} \approx 52$ [46] mg/cm^2.

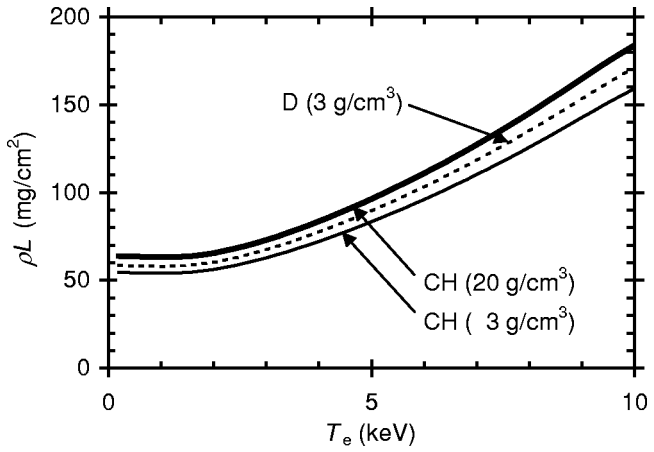

FIG. 34. $\langle \rho L \rangle$ required for ranging 14.7-MeV protons down to 12.7 MeV for different assumptions about plasma structure (calculated with the slowing-down formalism of Ref. 72). For densities and temperatures characterizing the material causing slowing down in the capsules under study, the deduced $\langle \rho L \rangle$ is relatively insensitive to assumptions about temperature, density, and chemical composition (most of the slowing down occurs in the shell, where T_e is on the order of 0.5–1 keV).

The knock-on method works with implosions of DT-filled capsules with CH shells because the ratio of yields of knock-on protons from the shell [reaction (11)] and primary neutrons from the fuel plays the same role as the yield ratio of Eq. (24) played for knock-on particles from the fuel. It can be shown[33] that

$$\langle \rho L \rangle_{\text{shell}} = 4.30 \times 10^5 (dY_{\text{KO-}p}/dE)/Y_{\text{DT-}n} \ \text{MeV mg/cm}^2, \tag{27}$$

where $dY_{\text{KO-}p}/dE$ is the yield per MeV in the spectrum. This method has the advantage of being independent of temperature and density. The yield per MeV for implosion 23445 [from Fig. 24(e)] was 2.6×10^9, and implies that $\langle \rho L \rangle_{\text{shell}} = 57$ mg/cm^2. In the case of the hot-spot model, $\langle \rho R \rangle_{\text{shell}} = \langle \rho L \rangle_{\text{shell}} = 57$ mg/cm^2. For the uniform model, the coefficient A_{sRL} can be estimated from the compression ratio *CR* (Sec. VI B 3) and other parameters to be about 0.81, implying $\langle \rho R \rangle_{\text{shell}} \approx 46$ mg/cm^2.

As described above for studies of $\langle \rho R \rangle_{\text{fuel}}$, both knock-on and secondary-proton methods have been used in studies of how different laser conditions affect implosion performance.[33,34,67] It was shown[33,34] that the knock-on method gives $\langle \rho R \rangle_{\text{shell}}$ values for DT-capsule implosions that are very similar to those obtained with the secondary-proton method for D_2-capsule implosions when the only difference is in the fuel composition.

D. Shock-generated proton yields and the time evolution of capsule areal density

Implosions of D^{3}He-filled capsules sometimes result in spectra of D^{3}He protons with two clearly separated peaks.[30,68] Most of the yield appears in a line that is downshifted in energy by an amount that reflects the areal density of the capsule at burn time, but if that line is downshifted enough (e.g., by 2 MeV) then a smaller line is often visible at an energy very close to the birth energy of 14.7 MeV. This line is downshifted by only a few hundred keV and represents a time ~400 ps before the burn time when a portion of the fuel is temporarily compressed and heated by a shock wave; measurement of the downshift provides an estimate of the total areal density at that point in time. New data on this

''shock yield,'' with special capsules, are also being used to study fuel/shell mix, as discussed in Ref. 68 and in the next section.

E. Fuel/shell mix

Experiments have been performed to investigate the mixing of fuel and shell materials at their interface, using capsules containing pure ^{3}He gas; the shells were made of CH, with total thickness 20 μm, but each contained a 1 μm sublayer of CD, offset from the inner shell surface by a different amount.[66–69,37] D ^{3}He protons are produced only if mixing occurs to the depth of the CD sublayer, so implosions of capsules with different CD offsets can be used to determine how much of the shell is involved in the mix. Measured spectra of protons indicate that $\sim$1 μm of the inner surface of the original shell is typically mixed into the fuel. Other information about the mix has been obtained by comparison of the data with simulations. This involves constructing a model of the radial distributions of temperature and density of fuel and shell materials, including an overlapping mix region, and varying the model parameters in order to match all of the diagnostic data including primary yields of charged particles and neutrons, secondary yields of protons, neutrons, and knock-ons, etc. Such modeling has indicated that a description of the mix region can be constrained relatively uniquely by the data.

F. Capsule implosion symmetry

One of the original goals of the charged-particle spectrometry program was the study of implosion symmetry at burn time,[26] and by utilizing up to ten spectrometers simultaneously (two CPSs and eight WRFs) it has recently been possible to obtain symmetry data for a number of types of implosions at OMEGA. Asymmetries in energy and yield have been observed, although they are not generally correlated with each other. Asymmetries in energy have been seen for primary 14.7 MeV protons from D^{3}He-filled capsules[35] and for secondary protons from room-temperature and cryogenic D_2-filled capsules.[34,35] Since there are no acceleration effects for fusion products from these types of implosions, the energy differences can be attributed to differing amounts of slowing down in the capsule plasma. Low-mode-number variations seen in $\langle \rho L \rangle_{\text{total}}$ (calculated from variations in the mean energies of proton spectra measured at different angles about the capsule) have been as large as $\pm 50\%$ about the average for capsules with thick CH shells, and often appear to be correlated with laser drive balance.[35] Evidence of higher-mode capsule structure can sometimes be seen within the shapes of individual spectra, because short-angular-wavelength variations in shell thickness result in different energy losses for different particles and contribute to greater linewidths. This is discussed in the context of 14.7 MeV protons from thick-shell D^{3}He-filled capsules in Ref. 35. For discussions of measurements of the linewidths of low-energy fusion products (3.5 MeV DT α and 3 MeV DD p) from capsules with low ρR, and their interpretation as indicators of shell thickness variations, see Refs. 24 and 25.

G. Slowing down of charged particles in plasmas

The first experimental verification of the general form of theories for the slowing down of charged particles in plasmas has been performed with measurements of charged-particle spectra from D^{3}He implosions.[31] This was accomplished with simultaneous measurements of spectra of four different fusion products (DD triton, D ^{3}He alpha, DD proton, and D ^{3}He proton). Use of the separate measurements made it possible to separate the effects of electrostatic acceleration and plasma slowing, to eliminate other variables, and to look at the important dependence of slowing theories on particle energy (since the measurements correspond to particle velocities both above and below the thermal electron velocities in the plasma).

VII. DISCUSSION

The sample data shown here represent a small fraction of the work that has been performed with the spectrometers, and techniques are being expanded to include new types of measurements and new types of capsule implosions. An important current focus is implosions of cryogenic D_2 capsules, where WRF spectrometers are used to study secondary protons. Spectral measurements of knock-on D and T will be important for future cryogenic DT capsules. In the mean time, charged-particle data continue to be used in conjunction with other diagnostic data in studies of how capsules with room-temperature gas fills perform under different laser conditions, and special room-temperature targets are being studied for additional insights into implosion behavior and diagnostic techniques. Of particular interest are ongoing studies bearing on fuel–shell mix, shock-generated yields, and implosion symmetry for both direct- and indirect-drive experiments at OMEGA. Looking toward the future, it is anticipated that charged-particle spectrometers will also play an important role in ICF experiments at the National Ignition Facility.[73,74]

ACKNOWLEDGMENTS

The authors would like to express their great appreciation for support by the engineering staff at LLE. The work described here was performed in part at the LLE National Laser Users' Facility (NLUF), and was supported in part by U.S. Department of Energy Contract No. DE-FG03-99SF21782, LLE subcontract No. PO410025G, LLNL subcontract No. B313975, the U.S. Department of Energy Office of Inertial Confinement Fusion under Cooperative Agreement No. DE-FC03-92SF19460, and the New York State Energy Research and Development Authority. Part of this work was also performed under the auspices of the U.S. Department of Energy by University of California Lawrence Livermore National Laboratory under Contract No. W-7405-Eng-48.

[1] V. W. Slivinsky, H. G. Ahlstrom, K. G. Tirsell, J. Larsen, S. Glaros, G. Zimmerman, and H. Shay, Phys. Rev. Lett. **35**, 1083 (1975).
[2] D. C. Slater and F. J. Mayer, Laser Interaction Related Plasma Phenomena **4B**, 603 (1976).
[3] R. A. Cover, J. J. Kubis, F. J. Mayer, and D. C. Slater, Appl. Phys. Lett. **33**, 222 (1978).

[4] R. Decoste and B. H. Ripin, Phys. Rev. Lett. **40**, 34 (1978).
[5] P. Wagli, T. P. Donaldson, and P. Ladrach, Appl. Phys. Lett. **32**, 638 (1978).
[6] Y. Gazit, J. Delettrez, T. C. Bristow, A. Entenberg, and J. Soures, Phys. Rev. Lett. **43**, 1943 (1979).
[7] S. Skupsky and S. Kacenjar, J. Appl. Phys. **52**, 2608 (1981).
[8] T. E. Blue and D. B. Harris, Nucl. Sci. Eng. **77**, 463 (1981).
[9] S. Kacenjar, L. Goldman, and A. Entenberg, Rev. Sci. Instrum. **52**, 831 (1981).
[10] S. Kacenjar, S. Skupsky, A. Entenberg, L. Goldman, and M. Richardson, Phys. Rev. Lett. **49**, 463 (1982).
[11] J. Delettrez, A. Entenberg, Y. Gazit, D. Shvarts, J. Virmont, T. Bristow, J. M. Soures, and A. Bennish, Nucl. Fusion **23**, 1135 (1983).
[12] T. E. Blue, J. W. Blue, J. S. Durham, D. B. Harris, A. S. Hnesh, and J. J. Reyes, J. Appl. Phys. **54**, 615 (1983).
[13] G. H. Miley, D. B. Harris, A. H. Bennish, D. R. Welch, and C. K. Choise, Laser Interaction Related Plasma Phenomena **6**, 263 (1984).
[14] R. J. Leeper, J. R. Lee, L. Kissel, D. J. Johnson, W. A. Stygar, and D. E. Hebron, J. Appl. Phys. **60**, 4059 (1986).
[15] S. Kacenjar, L. M. Goldman, A. Entenberg, and S. Skupsky, J. Appl. Phys. **56**, 2027 (1984).
[16] H. Azechi *et al.*, Appl. Phys. Lett. **49**, 555 (1986).
[17] S. J. Gitomer, R. D. Jones, F. Begay, A. W. Ehler, J. F. Kephart, and R. Kristal, Phys. Fluids **29**, 2679 (1986).
[18] M. D. Cable and S. P. Hatchett, J. Appl. Phys. **62**, 23113 (1987).
[19] W. A. Stygar *et al.*, Rev. Sci. Instrum. **59**, 1703 (1988).
[20] H. Nakaishi, N. Miyanaga, H. Azechi, M. Yamanaka, T. Yamanaka, M. Takagi, T. Jitsuno, and S. Nakai, Appl. Phys. Lett. **54**, 1308 (1989).
[21] M. H. Key *et al.*, Opt. Commun. **71**, 184 (1989).
[22] H. Azechi, M. D. Cable, and R. O. Stapf, Laser Part. Beams **9**, 119 (1991).
[23] S. N. Lapin, G. W. Cooper, L. Davis, J. E. Bailey, W. A. Stygar, A. Carlson, and P. Reyes, Rev. Sci. Instrum. **63**, 4895 (1992).
[24] A. P. Fews, M. J. Lamb, and M. Savage, Opt. Commun. **98**, 159 (1993).
[25] Y. Kitagawa *et al.*, Phys. Rev. Lett. **75**, 3130 (1995).
[26] R. D. Petrasso *et al.*, Phys. Rev. Lett. **77**, 2718 (1996).
[27] D. G. Hicks *et al.*, Rev. Sci. Instrum. **68**, 589 (1997).
[28] S. Cremer, C. P. Verdon, and R. D. Petrasso, Phys. Plasmas **5**, 4009 (1998).
[29] D. G. Hicks, Ph.D. thesis, Massachusetts Institute of Technology, Cambridge, MA, 1999.
[30] C. K. Li *et al.*, Phys. Plasmas **7**, 2578 (2000).
[31] D. G. Hicks *et al.*, Phys. Plasmas **7**, 5106 (2000).
[32] D. G. Hicks *et al.*, Phys. Plasmas **8**, 606 (2001).
[33] C. K. Li *et al.*, Phys. Plasmas **8**, 4902 (2001).
[34] F. H. Séguin *et al.*, Phys. Plasmas **9**, 2725 (2002).
[35] F. H. Séguin *et al.*, Phys. Plasmas **9**, 3558 (2002).
[36] J. A. Frenje *et al.*, Phys. Plasmas **9**, 4719 (2002).
[37] C. K. Li *et al.*, Phys. Rev. Lett. **89**, 165002 (2002).
[38] T. R. Boehly *et al.*, Opt. Commun. **133**, 496 (1997).
[39] C. K. Li *et al.*, Rev. Sci. Instrum. **68**, 593 (1997).
[40] R. L. Fleischer, P. B. Price, and R. M. Walker, *Nuclear Tracks in Solids, Principles and Applications* (University of California Press, Berkeley, 1975).
[41] B. G. Cartwright, E. K. Shirk, and P. B. Price, Nucl. Instrum. Methods **153**, 457 (1978).
[42] H. A. Kahn *et al.*, Nucl. Tracks Radiat. Meas. **7**, 129 (1983).
[43] S. A. Durrani and R. K. Bull, *Solid State Nuclear Track Detections, Principles, Methods and Applications* (Pergamon, New York, 1987).
[44] J. Charvat and F. Spurny, Nucl. Tracks Radiat. Meas. **14**, 447 (1988).
[45] P. M. Stafford *et al.*, Nucl. Tracks Radiat. Meas. **14**, 373 (1988).
[46] A. P. P. Fews, Nucl. Instrum. Methods Phys. Res. B **71**, 465 (1992).
[47] T. W. Phillips, M. D. Cable, D. G. Hicks, C. K. Li, R. D. Petrasso, and F. H. Seguin, Rev. Sci. Instrum. **68**, 596 (1997).
[48] A. Szydlowski *et al.*, Nucl. Instrum. Methods Phys. Res. B **149**, 113 (1999).
[49] C. Stoeckl *et al.*, Phys. Plasmas **9**, 2195 (2002).
[50] S. P. Regan *et al.*, Phys. Rev. Lett. **89**, 085003 (2002).
[51] L. M. Hively, Nucl. Fusion **17**, 873 (1977).
[52] Brookhaven National Laboratory, Internal Report BNL4000 (1970).
[53] Track Analysis Systems Ltd., H. H. Wills Physics Lab., Tyndall Ave., Bristol BS8 1TL, United Kingdom.
[54] J. F. Ziegler, J. P. Biersack, and U. Littmark, *The Stopping and Range of Ions in Solids* (Pergamon, New York 1985), Vol. 1.
[55] F. Ziegler and J. P. Biersack, SRIM, A code for calculations of the Stopping and Range of Ions in Matter, Jan. 1 2000, Version 0.05.
[56] J. A. Frenje *et al.*, Rev. Sci. Instrum. **73**, 2597 (2002).
[57] M. T. Collopy *et al.*, Rev. Sci. Instrum. **63**, 4892 (1992).
[58] A. Hussein, K. H. Shnishin, and A. A. Abou El Kheir, J. Mater. Sci. **28**, 6026 (1993).
[59] Dexter Corporation, Magnetic Materials Division (PERMAG), 48460 Kato Rd., Fremont, CA 94538.
[60] A. P. Fews and D. L. Henshaw, Nucl. Instrum. Methods **197**, 517 (1982).
[61] A. P. Fews, P. A. Norreys, F. N. Beg, A. R. Bell, A. E. Dangor, C. N. Danson, P. Lee, and S. J. Rose, Phys. Rev. Lett. **73**, 1801 (1994).
[62] F. N. Beg *et al.*, Phys. Plasmas **4**, 447 (1997).
[63] M. A. Russotto and R. L. Kremens, Rev. Sci. Instrum. **61**, 3125 (1990).
[64] J. P. Knauer, R. L. Kremens, M. A. Russotto, and S. Tudman, Rev. Sci. Instrum. **66**, 926 (1995).
[65] R. L. McCrory *et al.*, Nucl. Fusion **41**, 1413 (2000).
[66] R. D. Petrasso, Bull. Am. Phys. Soc. **43**, 1848 (1998).
[67] D. D. Meyerhofer *et al.*, Phys. Plasmas **8**, 2351 (2001).
[68] R. D. Petrasso *et al.*, Phys. Rev. Lett. (to be published).
[69] P. B. Radha *et al.*, Phys. Plasmas **9**, 2208 (2002).
[70] R. W. Short, J. M. Soures, W. Seka, D. G. Hicks, C. K. Li, and R. D. Petrasso, Bull. Am. Phys. Soc. **43**, 1881 (1998).
[71] R. D. Petrasso *et al.*, Bull. Am. Phys. Soc. **47**, 145 (2002); B. E. Schwartz *et al.*, Bull. Am. Phys. Soc. **47**, 219 (2002).
[72] C. K. Li and R. D. Petrasso, Phys. Rev. Lett. **70**, 3059 (1993).
[73] R. J. Leeper *et al.*, Rev. Sci. Instrum. **68**, 868 (1997).
[74] M. D. Cable *et al.*, Plasma Phys. Rep. **24**, 110 (1998).